Characterizing salt permeability in polyamide desalination membranes using electrochemical impedance spectroscopy

Devin L. Shaffer [a], Kathleen E. Feldman [b], Edwin P. Chan [b], Gery R. Stafford [b], Christopher M. Stafford [b]

submitted to *Journal of Membrane Science*

September 25, 2018

resubmitted February 26, 2019

[a] Civil and Environmental Engineering Department, University of Houston, 4726 Calhoun Road, Houston, TX 77204, USA

[b] Materials Science and Engineering Division, Material Measurement Laboratory, National Institute of Standards and Technology (NIST), 100 Bureau Drive, Gaithersburg, MD 20899, USA

[*] Corresponding author: C.M. Stafford, tel.: 301-975-4368; email: chris.stafford@nist.gov

Abstract

Improving the performance of desalination membranes requires better measurements of salt permeability in the polyamide separating layer to elucidate the thermodynamic and kinetic components of membrane permselectivity. In this work, electrochemical impedance spectroscopy (EIS) is introduced as a technique to measure the salt permeability and estimate the salt partition coefficient in thin polyamide films created using molecular layer-by-layer deposition. The impedance of supported polyamide films ranging in thickness from 3.5 nm to 28.5 nm were measured in different electrolyte solutions. Impedance spectra were modeled with equivalent circuits containing resistive and capacitive elements associated with the EIS measurement system as well as characteristic low-frequency parallel resistive and capacitive elements that are associated with the polyamide film. The characteristic polyamide membrane resistance increases with film thickness, decreases with solution concentration, and is an order of magnitude greater for a divalent cationic solution than for a monovalent cationic solution. For each polyamide film, salt permeability is calculated from the membrane resistance, and a salt partition coefficient is estimated. At the highest solution concentration measured, which is representative of brackish water desalination conditions, the calculated salt permeabilities range from $P_s = 1.3 \times 10^{-16}$ m s^{-1} to 3.9×10^{-16} m s^{-1}, and the estimated salt partition coefficients range from $K_s = 0.008$ to 0.016. These measurements demonstrate that EIS is a powerful tool for studying membrane permselectivity through the measurement of salt permeability in thin polyamide films.

Keywords: polyamide, membrane, electrochemical impedance spectroscopy, permeability

1   Introduction

Membrane materials with enhanced permselectivity are critical to expanding desalination applications by improving process performance and producing higher quality water [1], which translates to lower system energy consumption and associated costs [2]. The most common membranes used in desalination are thin-film composites (TFC) formed by interfacial polymerization of a thin polyamide selective layer on a porous polysulfone support layer [3]. In TFC membranes, transport is commonly described by a solution-diffusion model, wherein water flux, J_w (L m^{-2} h^{-1}), and salt flux, J_s (g m^{-2} h^{-1}), across the membrane are driven by hydraulic pressure and a concentration gradient, respectively [4]. Membrane permselectivity, α, defined as the ratio of membrane water and salt permeabilities, P_w and P_s, respectively, includes a thermodynamic component (partition coefficient, K) and a kinetic component (diffusion coefficient, D) [5], as described in Eq. 1.

$$\alpha = \frac{P_w}{P_s} = \frac{K_w D_w}{K_s D_s} \qquad\qquad\qquad\qquad (\text{Eq. 1})$$

Surface roughness and chemical heterogeneity complicate direct measurements of the intrinsic permeability and permselectivity of interfacially-polymerized polyamide selective layers [6]. Selective layer thickness is estimated to be in the range of 100 nm to 350 nm [7,8], though the actual continuous separating layer may only be 20 nm thick [9]. Furthermore, the transport properties of the selective layer and the support layer are often convoluted, further confounding direct measurement of water and salt permeabilities. As a result, engineering transport parameters, such as the water permeability coefficient, A (L m^{-2} h^{-1} bar^{-1}), and salt permeability coefficient, B (L m^{-2} h^{-1}), are commonly used to describe membrane permeability [5].

Recently, researchers have made advances in directly measuring water permeability, P_w (m^2 s^{-1}), in polyamide films by monitoring swelling or deswelling via atomic force microscopy [10], x-ray reflectivity [11,12], quartz crystal microbalance gravimetry [13], poroelastic relaxation indentation [14], and Fourier transform infrared spectroscopy [15]. Many of these studies were made possible by the molecular layer-by-layer (mLbL) deposition technique, which enables the fabrication of thin polyamide films with controlled thickness [16]. Molecular dynamics simulations have also been performed to estimate water permeability in polyamide membranes [17,18].

Salt permeability, P_s (m^2 s^{-1}), is more challenging to measure than water permeability because permeating salts represent a significantly smaller fraction of species in the swollen membrane. Salt permeabilities in the polyamide selective layers of commercial TFC desalination membranes and in polyamide films have been experimentally measured, typically from the perspective of salt partition coefficient, K_s, using pulsed nuclear magnetic resonance [19], atomic absorption spectroscopy [20], Rutherford backscattering spectroscopy [21], quartz crystal microbalance

gravimetry [22], and electrochemical impedance spectroscopy [23]. However, the salt partition coefficients from these experiments vary over three orders of magnitude, from K_s = 0.001 to 6.

Electrochemical impedance spectroscopy (EIS) shows promise as a technique to directly measure the salt permeability and estimate the salt partition coefficient in thin polyamide films. EIS measures the response of a system to an applied voltage as a function of frequency. Consequently, EIS can access processes happening at different characteristic frequencies and timescales, including salt permeability at the solution-diffusion timescale. The interpretation of the system impedance response can improve our understanding of the relative contributions of solubility and diffusivity to salt permeability. Previous work using EIS to study salt permeability in polyamide was challenged by the roughness and heterogeneity of the polyamide layer from a commercial desalination membrane [23]. Polyamide roughness affected the adhesion and contact area with the EIS system electrodes and violated the assumption of a smooth planar dielectric film that is the basis of the interpreting the EIS results. The mLbL deposition process overcomes these challenges by adhering smooth polyamide films with controlled thickness directly to substrates that can serve as electrodes [16]. Controlled polyamide films fabricated using the mLbL deposition technique have been used as model materials to study the structure, property, and performance relationships of desalination membranes [14,24–27]. In this work, salt permeability in polyamide is measured through EIS characterization of mLbL polyamide films. Permeability trends with solution concentration and polyamide film thickness are discussed in the context of the structure and properties of the polyamide film. Measured values are compared to reported results from other polyamide characterization techniques and to reported values for thin-film composite desalination membranes.

2   Experimental [28]

2.1   Molecular layer-by-layer (mLbL) deposition of polyamide films

Polyamide films were created directly on gold-coated silicon substrates (100 nm gold, Platypus Technologies, Madison, WI, USA) using a spin-assisted molecular layer-by-layer (mLbL) deposition technique [29] that involved sequential deposition of trimesoyl chloride (TMC, Sigma-Aldrich) monomer solution (1% by mass in toluene), toluene rinse, m-phenylenediamine (MPD, Sigma-Aldrich) monomer solution (1% by mass in toluene), and acetone rinse. Films were created with 3, 5, 10, 15, 30, 45, and 90 deposition cycles. After the mLbL deposition process, the polyamide films were annealed at 215 °C for 60 s.

A portion of each gold-coated silicon substrate was masked during the mLbL deposition process to enable subsequent electrode attachment. Prior to mLbL polyamide deposition, substrates (1 cm × 2 cm) were cleaned for 600 s in an ultraviolet/ozone cleaner (Jelight Co., Irvine, CA, USA). An area of 1 cm × 1 cm was masked with Kapton tape during the mLbL deposition process. After film deposition, the upper 5 mm of the masked 1 cm × 1 cm sample area was uncovered and used for soldering electrode connections. Stop-off lacquer was applied to protect

the soldered connection. A photograph of a representative polyamide film sample is shown in the inset of Figure 1.

Thicknesses of the dry polyamide film samples were measured using an optical profilometer (Zygo NewView 7200, Middlefield, CT, USA). Measured thicknesses are plotted versus number of mLbL deposition cycles in Figure 1. A linear fit to the data ($R^2 = 0.98$) has a slope of 0.30, indicating a polyamide film growth rate of 0.30 nm per mLbL deposition cycle. This growth rate is consistent with the rates of 0.34 nm per cycle [29] and 0.32 nm per cycle [11] previously reported for TMC/MPD polyamide films fabricated using the spin-assisted mLbL deposition technique. Measured thicknesses of 3-cycle and 5-cycle films are approximately equal at 3.5 nm $\pm$ 0.3 nm and 3.4 nm $\pm$ 0.3 nm, respectively. The equivalent film thicknesses could be the result of contamination on the films, film densification, or subtle variations in the mLbL deposition process. Greater variability in the thickness measurements for higher cycle-number films could be the result of interference from the masked area during film deposition.
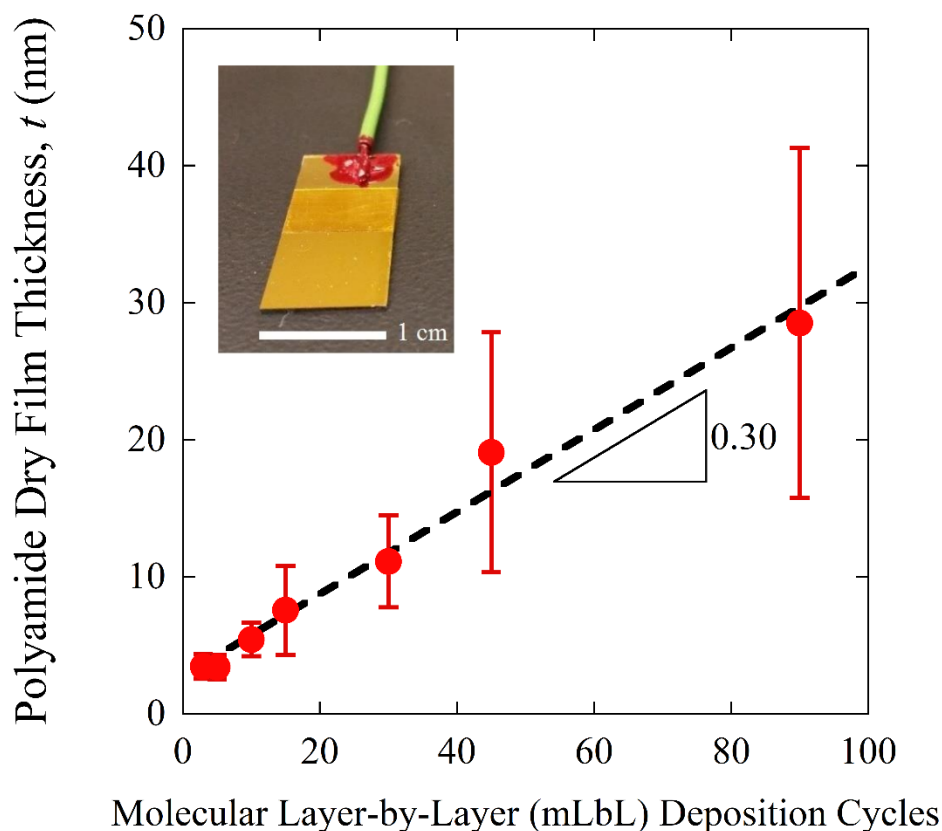

Figure 1 – Polyamide dry film thickness, *t,* as a function of number of cycles in the molecular layer-by-layer (mLbL) deposition process. Inset is a photograph of a typical polyamide film

sample on a gold-coated silicon working electrode with soldered electrode connection sealed with red stop-off lacquer.

2.2   *Electrochemical impedance spectroscopy (EIS) measurements*

Electrochemical impedance spectroscopy (EIS) was conducted with an AutoLab potentiostat (Model PGSTAT 302, Metrohm USA Inc., Riverview, FL, USA), and the associated NOVA software (v.1.9) was used for equivalent circuit modeling. Impedance measurements were made in a three-probe cell configuration with the gold-coated silicon substrate upon which polyamide films were deposited serving as the working electrode. Counter and reference electrodes were constructed of platinum, the latter because of its low impedance. Before and after each impedance measurement, the platinum reference electrode was referenced to a saturated mercury-mercurous sulfate electrode (SSE), a standard reference electrode for electrochemical measurements. The SSE reference electrode has a potential of +0.64 V vs the standard hydrogen electrode (SHE), the current standard for zero potential. The SSE was placed inside an electrolyte-filled capillary that was fitted with a vycor tip and inserted into the measurement cell. A schematic and photograph of the three-probe cell are shown in Figure 2.
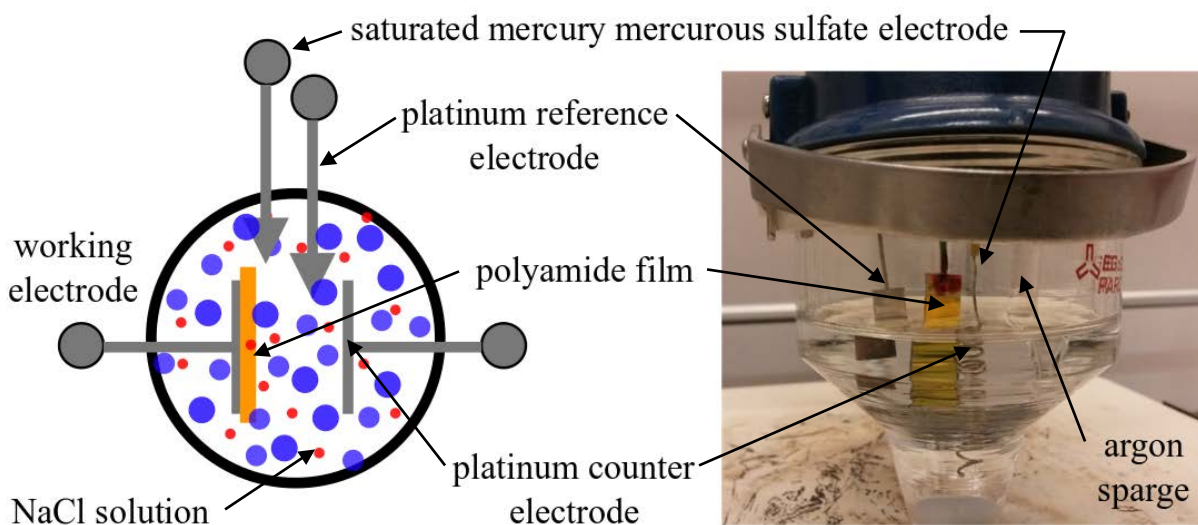

Figure 2 – Schematic and photograph of the three-probe cell used to make electrochemical impedance spectroscopy measurements.

A voltammetric sweep was initially conducted to determine the fixed potential at which to make EIS measurements, and the voltammogram is shown in Figure S1 of the Supporting Information. A fixed potential of approximately -0.4 V with respect to SSE was chosen to avoid Cl⁻

adsorption [30] and O_2 reduction [31] at the gold electrode surface, which occurred at approximately -0.1 V SSE and between -0.6 V SSE to -1.0 V SSE, respectively. As detailed in Section S1 and Figure S2 of the Supporting Information, the minimum electrochemical interference occurs at a potential of -0.4 V SSE, where the impedance of the gold-coated silicon working electrode is modeled as an equivalent electrical circuit with solution resistance and double layer capacitance in series.

EIS measurements were made for a bare gold electrode and for each polyamide film thickness in NaCl (J.T. Baker) solution concentrations of 3.2 mmol L^{-1}, 10 mmol L^{-1}, 32 mmol L^{-1}, and 100 mmol L^{-1}. Experiments with NaCl solutions allow for comparison to previous studies of salt permeability using NaCl and to reported NaCl salt permeability coefficients for commercial polyamide desalination membranes. Additional measurements were made in 50 mmol L^{-1} Na_2SO_4, 50 mmol L^{-1} $MgCl_2$, and 50 mmol L^{-1} $MgSO_4$ (Sigma-Aldrich) solutions. The selected solution concentrations represent a range of total dissolved solids concentrations that is relevant to brackish water reverse osmosis and that enables the study of both Donnan and non-Donnan components of total ion partitioning. The lowest NaCl solution concentration of 3.2 mmol L^{-1} was selected to avoid measurement artifacts that were apparent for lower solution concentrations due to the high impedance of the system. Samples were equilibrated in each solution for a minimum of 12 h before measurement, and NaCl measurements were made in the order of increasing NaCl solution concentration. Solutions were sparged with argon gas for approximately 1 h before measurement to remove dissolved oxygen. The EIS measurements for each sample interrogated 50 frequencies in the range 0.01 Hz to 200 kHz using a potential amplitude of 10 mV RMS (root mean square) and -0.4 V fixed potential with respect to SSE. The measured impedance spectra were modeled with equivalent electrical circuits containing resistive and capacitive (constant phase) elements.

3   Results

3.1   Impedance spectra of mLbL polyamide films

In an EIS experiment, the system responds to the application of a sinusoidal signal. The ratio of the input ac voltage to the output ac current is a complex quantity called the electrochemical impedance, Z:

$$Z = Z_0 \exp(-j\phi) \tag{Eq. 2}$$

where Z_0 is the magnitude of the impedance (equal to the amplitude of the potential divided by the amplitude of the current), $j = \sqrt{-1}$, and ϕ is the phase angle of the current with respect to the potential. The complex impedance Z comprises a real component ($Z' = Z_0(cos\phi)$) and an imaginary component ($Z'' = Z_0(jsin\phi)$). We use the convention that a signal that lags the input signal has a negative phase angle. As shown in Eq. 2, the electrochemical impedance has a negative phase angle, which is consistent with standard electrochemical convention. The

impedance is typically represented in the form of Bode plots, where Z_0 and ϕ are plotted as a function of frequency in Hz.
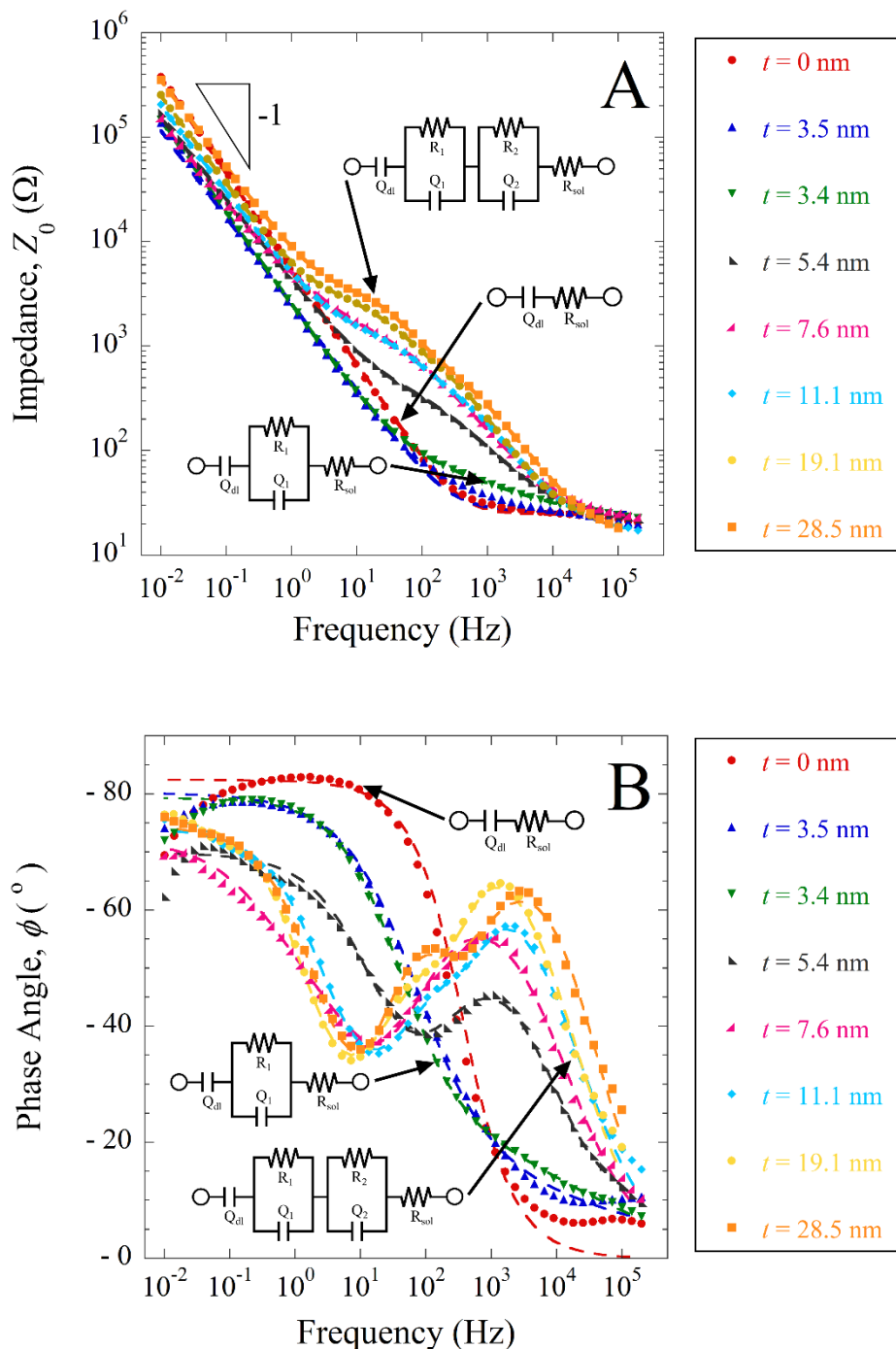

Figure 3 – Bode plots comparing A) impedance, Z_0, and B) phase angle, ϕ, for all polyamide film thicknesses measured in 100 mmol L^{-1} NaCl solution (symbols) with modeled impedance and phase angle from equivalent circuit fits (dashed lines). Representative [$R_{sol}Q_{dl}$], [$R_{sol}Q_{dl}(RQ)_1$],

and [$R_{sol}Q_{dl}(RQ)_1(RQ)_2$] equivalent circuits are illustrated, and the corresponding impedance and phase angle fits are indicated.

Representative impedance spectra for all polyamide film thicknesses measured in 100 mmol L^{-1} NaCl solution are shown in the Bode plots in Figure 3. The Bode plots illustrate both capacitive and resistive behavior in Z_0 and ϕ. Capacitive behavior is indicated by a slope of -1 on the Bode plot and a phase angle of -90^0. Resistive behavior is indicated by a slope of 0 on the Bode plot and a phase angle of 0^0.

3.2   Equivalent circuit models

Different equivalent electrical circuits were used to model the impedance spectra of the polyamide films. Constant phase elements, Q, were used instead of capacitors, C, in all of the equivalent circuit models in order to better fit the impedance spectra. Constant phase elements represent non-ideal or "leaky" capacitors. The non-ideality of constant phase elements has been attributed to electrode surface heterogeneities occurring on the atomic scale, inhomogeneity of barrier film properties, and non-uniform distributions of potential and current [32]. The impedance of a constant phase element, Z_Q, is defined in Eq. 3.

$$Z_Q = \frac{1}{Y_Q(j\omega)^n} \qquad\qquad\qquad \text{(Eq. 3)}$$

where Z_Q is the impedance of the constant phase element Q

Y_Q (S s^n) is the admittance of the constant phase element at $\omega = 1$ rad s^{-1}

j is the imaginary unit, where $j^2 = -1$

ω is the radial frequency (rad s^{-1}), equal to $2\pi f$ (f is the frequency in Hz)

n is an exponent indicating the deviation from pure capacitive behavior (at $n = 1$, Y_Q is equivalent to capacitance C)

For the bare gold electrode ($t = 0$ nm), an equivalent circuit with a single resistor, R, and constant phase element, Q, in series [RQ] was used to fit the impedance response. We use the convention that circuit elements in brackets [ ] are in series while those in parentheses ( ) are in parallel. For the [RQ] circuit for the bare gold electrode, the resistor describes solution resistance, R_{sol}, and can be obtained from the impedance data at high frequency where the impedance of Q is near zero. The constant phase element represents the double-layer capacitance, Q_{dl}, of the gold working electrode.

Resistors or constant phase elements were added to the equivalent circuit to model the increasingly complex response of polyamide films with increasing thickness. For the 3-cycle mLbL polyamide film ($t = 3.5$ nm) and 5-cycle film ($t = 3.4$ nm), a resistor and constant phase element in parallel (RQ) were added to the equivalent circuit [$R_{sol}Q_{dl}(RQ)$]. Though the 3-cycle and 5-cycle films are nominally the same thickness, qualitative differences are apparent in their

S9

impedance spectra at high frequencies. Polyamide films equal to or greater than 10 mLbL cycles (5.4 nm $\leq t \leq$ 28.5 nm) were modeled with two parallel resistors and constant phase elements in series with solution resistance and double-layer capacitance [$R_{sol}Q_{dl}(RQ)_1(RQ)_2$]. The different equivalent circuit models and their associated fits to the impedance spectra are shown in Figure 3.

3.3   Representing measurement uncertainty
Uncertainty in the measurement of polyamide dry film thicknesses is represented by reporting the mean and displaying the standard deviation of the mean as error bars in all figures. Standard errors of resistors and constant phase elements in equivalent circuit models were determined by NOVA software for each equivalent circuit fit. For resistors, the reported standard error is used and graphically represented as error bars. Calculations of salt permeabilities and salt permeability coefficients used the membrane resistance values from equivalent circuit fits and the measured polyamide film dry thicknesses. Uncertainties in the resistive element fits and the measured film thicknesses were propagated through the permeability calculations to calculate a standard deviation for the salt permeabilities and salt permeability coefficients [33].

Uncertainties in capacitances for the equivalent circuit models were quantified using a statistical approach. Capacitances were calculated from constant phase elements in parallel with resistors using a procedure developed by Mansfield [34], as described in Section 4.3, and the values of these resistors and constant phase elements were determined by NOVA fitting software with associated standard errors. To estimate the standard error for each capacitance, a population of 10,000 representative capacitance values was calculated from iterations of resistances and Y_Q and *n* values for constant phase elements that were randomly sampled from a range represented by the mean ± standard error from the NOVA fit. From the population of representative capacitance values, a mean and standard error were calculated. The statistically-determined standard error is used with the capacitance value calculated according to Section 4.3.

4   Discussion
4.1   Solution resistance and electrode double-layer capacitance
The equivalent circuit models used to fit the impedance spectra of polyamide film samples include solution resistance, R_{sol}, and working electrode double layer capacitance, Q_{dl}, elements that are associated with the measurement system. Additional resistors and constant phase elements in the equivalent circuit models are associated with the polyamide film. A more detailed discussion of distinguishing the impedance response of the polyamide film from that of the bare gold-coated silicon electrode is included in Section S2 and Figure S3 of the Supporting Information.

Solution resistances are apparent at high frequencies in the impedance spectra, and equivalent circuit fits for measured solution resistances at different NaCl solution concentrations are plotted

as a function of polyamide film thickness in Figure 4A. In Figure 4A, R_{sol} values have been normalized to polyamide film area and have units of Ω-cm^2. Solution resistance shows a slight decreasing trend with increasing polyamide film thickness. Although solution resistance is expected to be constant for each NaCl solution concentration and independent of membrane thickness, the impedance data in Fig. 3(A) shows that the high frequency impedance of the membrane covered electrodes are typically lower that of the pure gold electrode ($t = 0$ nm). There is presently no clear explanation for this trend. Variations in the positioning of the reference electrode may influence the measured values of R_{sol}, however, such variations would be random and would not scale with membrane thickness. Another possibility is that the presence of the membrane alters the current distribution between the working and counter electrodes, which in turn influences the potential drop between the working and reference electrodes from which R_{sol} is determined. Future work will include modeling the primary current distribution under the experimental conditions examined here to determine if this is a viable cause for the observed decrease in R_{sol} with membrane thickness. It should be noted that a varying current distribution in the electrolyte will only influence the measured values of R_{sol}. It will not impact the circuit elements representing the membrane and the gold-coated silicon electrode surface.

As expected, R_{sol} decreases with increasing NaCl solution concentration. The predicted relationship between solution resistivity and increasing NaCl concentration is a power law decay with an exponent of -0.968 [35], and the measured relationship for R_{sol} exhibits power law decay with an exponent of -0.887, as shown in Figure S4 of the Supporting Information. The electrochemical cell used in this study does not confine the current distribution between the working and counter electrodes, nor is the reference electrode placed in a suitable position that would allow the measured R_{sol} values to be converted into specific resistivity that could then be compared to literature values. However, resistivity measurements were made with selected NaCl solutions using EIS and a conductivity cell with a known cell constant. These data are plotted with reference values [35] in Fig. S4, and the agreement is excellent.

Capacitive behavior due to the double layer is apparent at low frequencies in the impedance spectra. Admittance values, Y_Q, of the constant phase elements associated with double layer capacitance are plotted in Figure 4B as a function of polyamide film thickness for different NaCl solution concentrations. Admittance Y_Q has also been normalized to polyamide film area and has units of S s^n cm^{-2}.

Admittance values (equivalent to capacitance for exponent $n = 1$) are approximately 1×10^{-5} S s^n cm^{-2} for the bare gold electrode. The admittance increases into the range 2×10^{-5} S s^n cm^{-2} to 8×10^{-5} S s^n cm^{-2} when the polyamide film is present. The admittance values are highest for films less than 10 nm thick. The origin of this admittance increase is likely associated with charged groups in the polyamide, such as free carboxylic acid groups, in the proximity of the gold surface that increase the overall capacitance. Whether the film is present or not, the double

S11

layer admittance increases with increasing NaCl solution concentration. This behavior is consistent with a reduction in Debye length, κ^{-1} (nm), for simple dielectric behavior in electrolyte solutions.
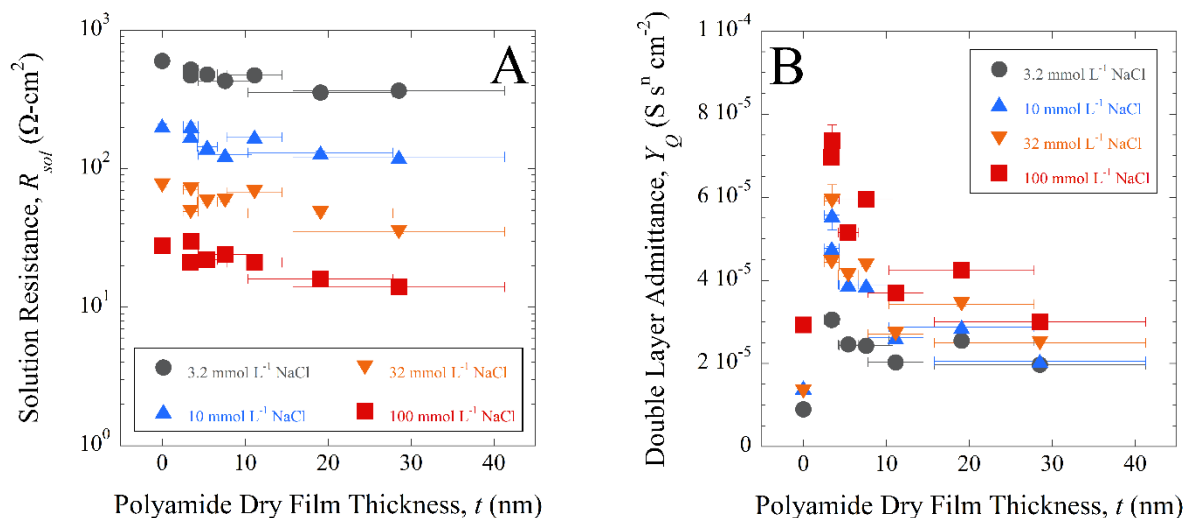

Figure 4 – A) Modeled solution resistance, R_{sol}, as a function of polyamide film thickness, t, for different NaCl solution concentrations and B) modeled constant phase element admittance, Y_Q, representing double layer capacitance as a function of polyamide film thickness, t, for different NaCl solution concentrations.

4.2   Equivalent circuit models reflect mLbL polyamide film growth

The impedance associated with the polyamide film is observed at intermediate frequencies between low-frequency double-layer capacitance and high-frequency solution resistance. This impedance response changes with increasing polyamide film thickness, as illustrated in the Bode plots in Figure 3. As the polyamide film thickness increases from 0 nm to 3.4 nm, a single (RQ) element develops in the impedance spectra, as shown by a single plateau in the Bode plot of Z_0 and a relatively small peak in the Bode plot of ϕ for film thickness $t = 3.4$ nm at frequency range 10^3 Hz to 10^4 Hz. For thicker polyamide films (7.6 nm $\leq t \leq$ 28.5 nm), the (RQ) element impedance response is more pronounced with larger impedance magnitudes in the plateau region and larger associated changes in the phase angle. Ultimately, two prominent plateaus develop in the Bode plot of Z_0 for the thickest films. Two corresponding large peaks appear in the phase angle Bode plot at frequencies ranging from 10^1 Hz to 10^4 Hz, indicating two (RQ) elements in series.

The changes in impedance with increasing film thickness reflect the growth of the polyamide film via the mLbL deposition process. Recent work used swelling ratio measurements to

demonstrate that mLbL polyamide network properties change as a function of thickness, as the void space fraction is reduced in the growing polyamide film [11]. The void space fraction in the smooth mLbL polyamide films is indicative of the network properties and is different from the nanobubbles observed in the polyamide selective layers of commercial interfacially-polymerized desalination membranes [9]. The swelling study is consistent with the view that the void space fraction in the growing mLbL polyamide films is reduced with increasing deposition cycles [11]. Another recent study using Fourier transform infrared spectroscopy to quantify free carboxylic acid content in mLbL polyamide films observed that carboxylic acid content decreased as film thickness increased, indicating increased crosslink density for thicker films [27]. The thickness dependence of measured polyamide film impedances in this work suggests that polyamide films less than approximately 10 nm thick have relatively larger void space fractions and lower crosslink densities than films thicker than approximately 10 nm.

In previous EIS studies of interfacially-polymerized polyamide films [23,36], an equivalent circuit with a single (RQ) time constant associated with the polyamide film was used to model the impedance data. In this work, the presence of two prominent (RQ) elements in the impedance response of polyamide films thicker than approximately 10 nm is attributed to the mLbL fabrication process. As described in the mLbL polyamide swelling ratio study [11], the mLbL polyamide growth process is hypothesized to result in a two-layer polyamide network structure: initially-deposited polyamide layers have a higher void space fraction and polyamide layers deposited later have a lower void space fraction. The resulting polyamide films may have different network properties as a function of film thickness. We attribute two (RQ) elements in the equivalent circuit models for thick mLbL polyamide films to this hypothesized two-layer network structure.

4.3   Distinguishing resistive and capacitive elements associated with the polyamide film
A capacitance, C, was calculated for each of the parallel resistor and constant phase element components (RQ) associated with the polyamide films in the equivalent circuit models, using a conversion developed by Mansfield [34], as shown in Eq. 4:

$$C = Y_Q\left(\omega_m^{"}\right)^{n-1}$$
(Eq. 4)

where $\omega_m^{"}$ is the frequency at which the imaginary impedance is maximum, which was determined graphically.

Using this calculated capacitance and the modeled resistance, a characteristic frequency, f_c, was calculated from Eq. 5 for each parallel (RQ) element associated with the polyamide film.

$$f_c = \frac{1}{2\pi RC}$$
(Eq. 5)

S13

The resulting characteristic frequencies are shown in Figure 5 for EIS measurements of polyamide film thicknesses in different solutions and solution concentrations. The characteristic frequencies cluster into a high-frequency (RQ) element and a low frequency (RQ) element for each polyamide film thickness that was modeled with two (RQ) elements in series. These high- and low-frequency elements are apparent for measurements made in both monovalent and divalent cation solutions. Polyamide films less than 10 nm thick did not yield coherent f_c values associated with the high-frequency (RQ) element, and only the low-frequency f_c values are shown for these films in Figure 5.
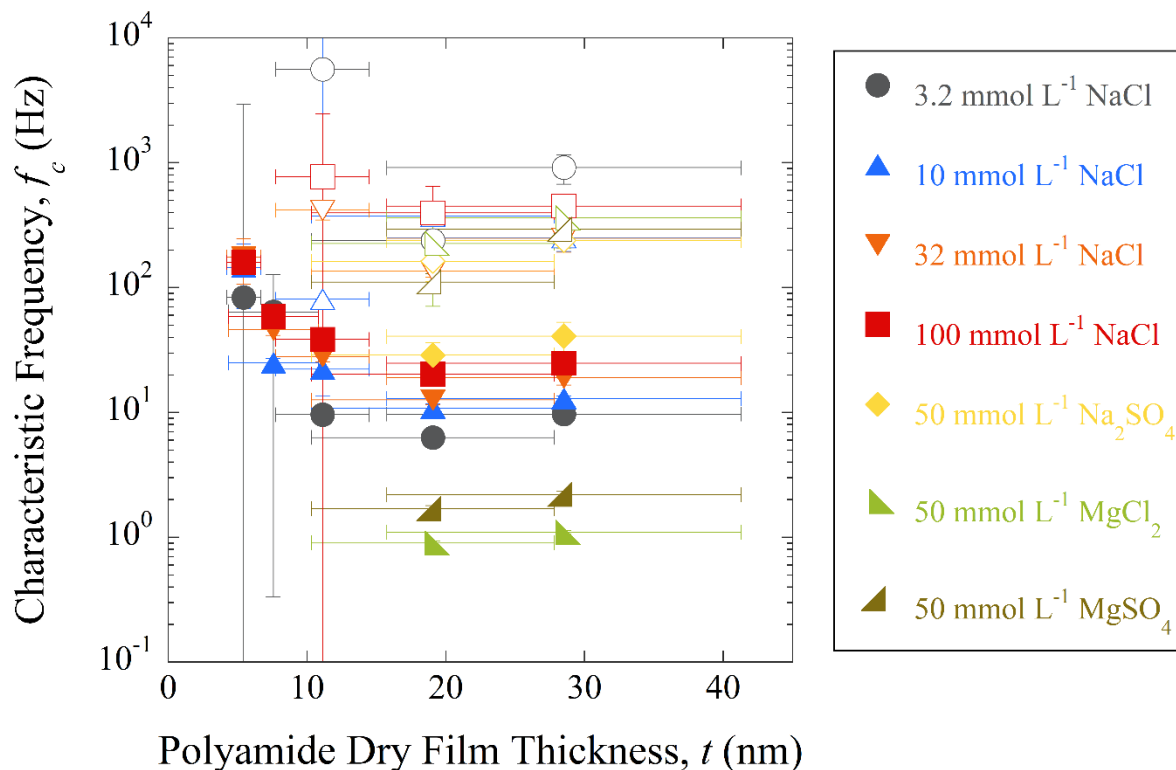

Figure 5 – Calculated characteristic frequencies, f_c, of high-frequency parallel (RQ) elements (open symbols) and polyamide film-related low-frequency parallel (RQ) elements (closed symbols) as a function of polyamide film thickness, t, for different salt solutions. Symbols represent different NaCl solution concentrations and different divalent salt solutions used in the measurements.

The low-frequency (RQ) element f_c values decrease with increasing film thickness to approximately 11 nm, and then the f_c values plateau. The plateau in f_c with increasing thickness is a result of the observed plateau in resistance measurements, as discussed in Section 4.4. The low-frequency (RQ) element is attributed to the polyamide film because it is consistent with a slowing (RQ) response as film thickness and associated resistance increase. As discussed in

Sections 4.4, 4.5, and 4.6, the polyamide film resistance governs the characteristic frequency response. Thus, the resistance R associated with the low-frequency (RQ) elements and the associated calculated capacitance C are subsequently defined as membrane resistance, R_{mem}, and membrane capacitance, C_{mem}. High-frequency (RQ) elements could be associated with inhomogeneities in the void space fraction of the polyamide film because of the mLbL deposition process, as discussed in Section 4.2, and these high-frequency (RQ) elements may contain structural information about the polyamide films. However, these elements show no strong correlation to film thickness or solution concentration, indicating that they are of secondary importance for this study.

4.4 Effect of film thickness on membrane resistance and capacitance

The membrane resistance and capacitance values are shown as a function of polyamide thickness in Figure 6. These values are normalized to polyamide film area. Membrane resistance increases with increasing polyamide film thickness, as expected for a dielectric layer, for films less than approximately 19 nm thick. For films thicker than approximately 19 nm, the value of R_{mem} appears to plateau; however, there is no clear physical reason to observe a plateau in R_{mem}, as one would expect R_{mem} to increase with increasing thickness of the film. The observed plateau in R_{mem} might be due to variability in measured thicknesses for the higher-cycle number mLbL polyamide films. The relatively high variability in measured thickness for the thickest polyamide film ($t = 28.5$ nm) may be influencing the appearance of a plateau in R_{mem} values with increasing film thickness. Membrane capacitances are in the range $C_{mem} = 1.5 \times 10^{-6}$ F cm^{-2} to 4.1×10^{-6} F cm^{-2}, and the C_{mem} values do not change significantly with film thickness, indicating that membrane capacitance does not follow simple, thickness-dependent dielectric behavior [23].
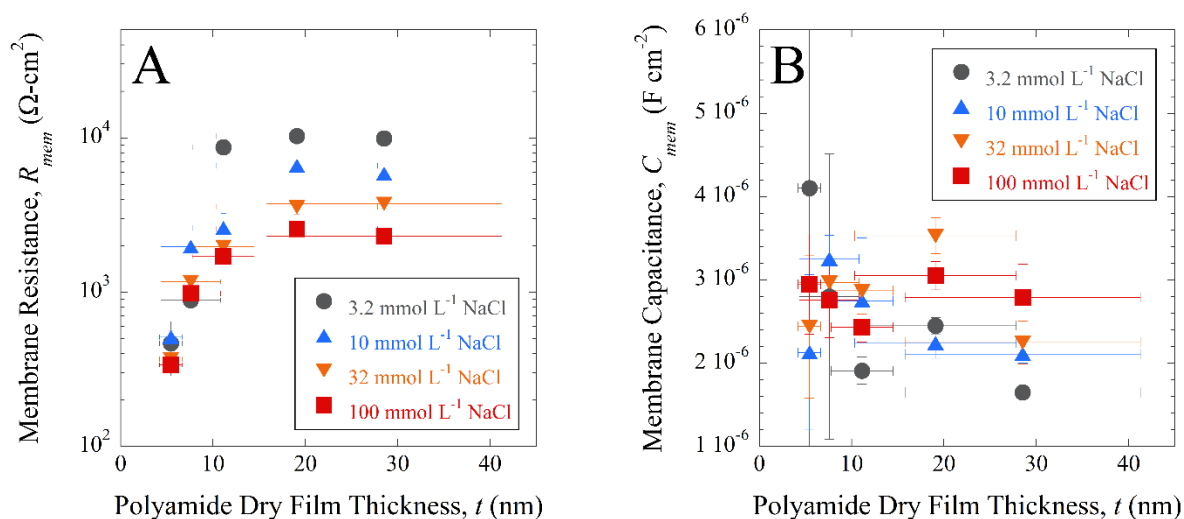

Figure 6 – A) Modeled membrane resistance, R_{mem}, and B) calculated membrane capacitance, C_{mem}, as functions of polyamide film thickness, t, for different NaCl solution concentrations.

4.5   Effect of solution concentration on membrane resistance and capacitance
Membrane resistance decreases with increasing solution concentration, as expected for a swollen polyamide film in equilibrium with NaCl solution. The dependence of R_{mem} on NaCl solution concentration is shown in Figure 6A and is most pronounced for thicker polyamide films ($t >$ 10 nm). Thin polyamide films ($t < 10$ nm) may have a relatively large void space fraction and low crosslink density, as discussed in Section 4.2, and under these circumstances, only the thicker polyamide films contain electrolyte solution in the polymer network void spaces that is distinct from the bulk solution. Thus, R_{mem} for thicker films ($t > 10$ nm) is sensitive to NaCl solution concentration, whereas changes in solution concentration are primarily reflected in the bulk solution resistance for thin polymer films ($t < 10$ nm). A strong dependence of polyamide membrane resistance on solution concentration has also been shown in a previous EIS study using commercial polyamide desalination membranes [23]. Membrane capacitances are not strongly affected by solution concentration, as shown in Figure 6B.

To isolate the polyamide resistance from the effect of solution concentration, a membrane resistivity, ρ_{mem} (Ω-cm), was calculated by normalizing R_{mem} for each polyamide sample to the dry polyamide film thickness ($\rho_{mem} = R_{mem} / t$). Membrane resistivity at 0 mmol L^{-1} NaCl solution concentration was extrapolated from linear fits to log-log plots of resistivity versus solution concentration for each polyamide film thickness, as shown in Figure S5 of the Supporting Information. The resulting ρ_{mem} values at 0 mmol L^{-1} NaCl solution concentration are summarized in Table S1 and are distinct for films thinner and thicker than 10 nm. For thin polyamide films ($t < 10$ nm), $\rho_{mem} < 2 \times 10^9$ Ω-cm at 0 mmol L^{-1} NaCl solution concentration. The resistivities of thicker films ($t > 10$ nm) are in the range $\rho_{mem} = 5 \times 10^9$ Ω-cm to 10×10^9 Ω-cm. These distinctive resistivities for polyamide films thinner and thicker than 10 nm further indicate that polyamide films created by the mLbL deposition process have different network properties at thicknesses less than or greater than a threshold of approximately 10 nm. The lower membrane resistivity observed for thin films, independent of solution concentration, may result from the reported greater concentrations of free carboxylic acid in thinner mLbL polyamide films compared to thicker films [27].

4.6   Effect of solute charge on membrane resistance and capacitance
Membrane resistances for monovalent and divalent cation solutions are compared in Figure 7 for the two thickest polyamide films studied ($t = 19.1$ nm and $t = 28.5$ nm).   Membrane resistance in divalent cationic solution (Mg^{2+}) is an order of magnitude greater than resistance in monovalent cationic solution (Na^+) at the same anion concentrations (Cl^- and SO_4^{2-}). At the divalent cation solution concentrations of 50 mmol L^{-1}, R_{mem} values are approximately an order of magnitude greater than R_{mem} values for monovalent cation solutions at both 32 mmol L^{-1} and 100 mmol L^{-1} concentrations, as shown in Figure 6, indicating that the differences in R_{mem} are not the result of cation concentration. The different R_{mem} values reflect the difference in size and water pair interaction energy of these hydrated cations [37,38]. Solution-diffusion transport of larger

hydrated divalent Mg^{2+} ions through the polyamide film will be reduced compared to smaller monovalent Na^+ ions [39], which is expressed in EIS measurements as a higher membrane resistance. Membrane capacitance values, which are also shown in Figure 7, are not strongly affected by solute charge, reinforcing the conclusion that membrane resistance dominates the characteristic (RC) behavior of the polyamide films.

At equivalent cation concentrations (50 mmol L^{-1} Mg^{2+} for $MgCl_2$ and $MgSO_4$, 100 mmol L^{-1} Na^+ for NaCl and Na_2SO_4), R_{mem} is greater for Cl^- salts than for SO_4^{2-} salts. This result is unexpected based on the smaller hydrated size and reduced hydration free energy of the Cl^- anion compared to the SO_4^{2-} anion [38]. A more detailed study of cation and anion charge effects on salt permeability is planned for future work.
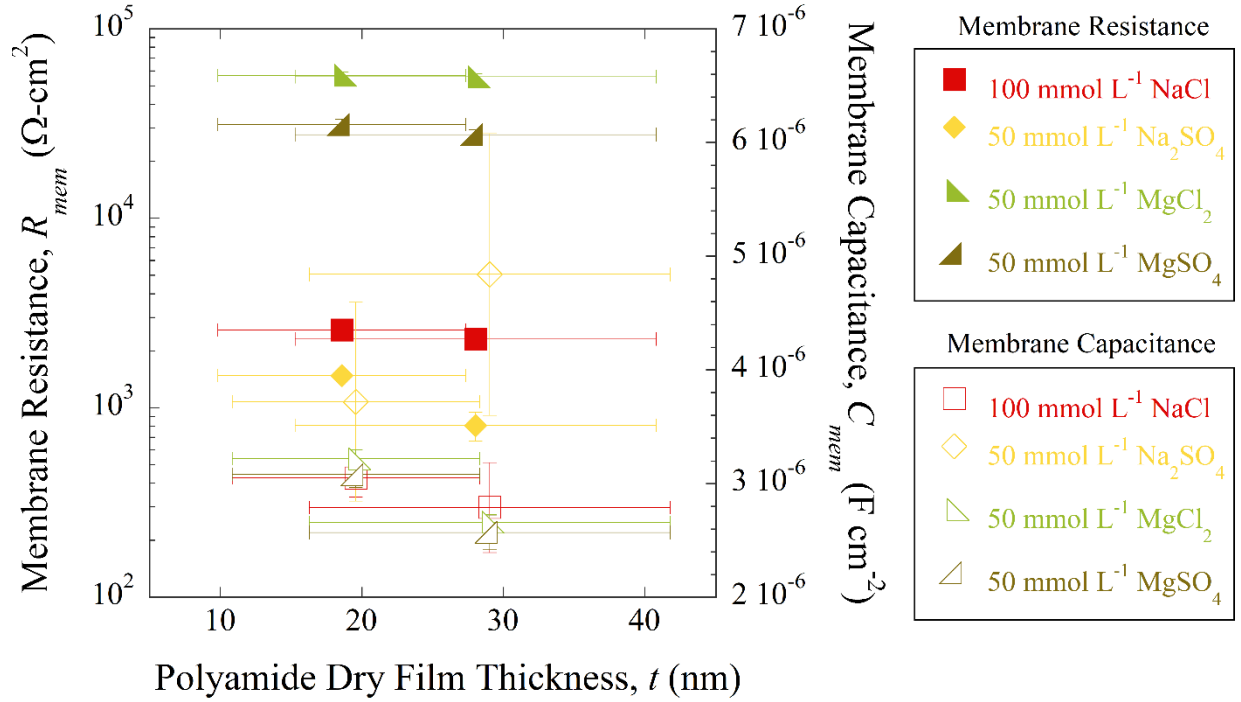

Figure 7 – Modeled membrane resistance, R_{mem}, (left vertical axis, closed symbols) and calculated membrane capacitance, C_{mem}, (right vertical axis, open symbols) for two polyamide film thicknesses, t. Symbols represent measurements made in different salt solutions.

4.7   Characterizing salt partitioning from membrane resistance

Total ion partitioning ΣK into the polyamide films can be characterized from the measured membrane resistance R_{mem} values according to Eq. 6, which assumes that the films behave as planar homogeneous dielectric layers [36] and that salt solutions are symmetrical with equivalent partition and diffusion coefficients for both anion and cation.

$$\sum K = \frac{t}{D_s c_s R_{mem}} \frac{RT}{F^2} \tag{Eq. 6}$$

where c_s is NaCl solution concentration

R is the universal gas constant

T is absolute temperature (295 K)

F is Faraday's constant

For weakly charged films like negatively charged polyamide desalination membranes [39], the total ion partitioning ΣK describes partitioning by cation counter-ions ($K_{counter}$) and by anion co-ions (K_{co}). Counter- and co-ion partitioning includes contributions from charge-based Donnan effects and from non-Donnan effects, which have been modeled by Yaroshchuck and Ribitsch [40] according to Eq. 7, Eq. 8, and Eq. 9.

$$K_{counter} = \sqrt{\left(\frac{X_{mem}}{2c_s}\right)^2 + K_s^2} + \left(\frac{X_{mem}}{2c_s}\right) \tag{Eq. 7}$$

$$K_{co} = \sqrt{\left(\frac{X_{mem}}{2c_s}\right)^2 + K_s^2} - \left(\frac{X_{mem}}{2c_s}\right) \tag{Eq. 8}$$

$$\sum K = K_{counter} + K_{co} = 2\sqrt{\left(\frac{X_{mem}}{2c_s}\right)^2 + K_s^2} \tag{Eq. 9}$$

The Donnan components of total ion partitioning ΣK are described by the fixed membrane charge concentration (X_{mem}) and are controlled by the ratio of fixed membrane charge and solution concentration ($X_{mem}/2c_s$). The non-Donnan component of ΣK includes dielectric effects such as image forces and Born effects [41] and is indicated by the parameter K_s. This non-Donnan partitioning is the salt partition coefficient K_s that is typically associated with solution-diffusion modeling of polyamide membranes used for desalination [36].

At relatively large $X_{mem}/2c_s$ ratios, such as the measurements made in low NaCl solution concentrations in this work, non-Donnan dielectric effects are screened, and ΣK can be approximated as the Donnan partitioning of counter-ions into the charged polyamide film ($\Sigma K \approx K_{counter} \approx (X_{mem}/2c_s)$). In this case, ΣK decreases with increasing solution concentration, and the resulting salt permeability also decreases, which has been previously observed by Rutherford backscattering spectroscopy [21], quartz crystal microbalance [22], EIS [23], and molecular dynamics [42] techniques.

When the X_{mem}/c_s ratio is relatively small, non-Donnan dielectric effects become significant, and ΣK can be approximated by the non-Donnan partitioning of counter-ions and co-ions into the polyamide film due to dielectric effects ($\Sigma K \approx 2K_s$). At a sufficiently high solution concentrations, the Donnan partitioning due to fixed membrane charges is screened, and ΣK approaches a constant non-Donnan salt partition coefficient $2K_s$. This behavior has been observed in the previously mentioned EIS [23] and quartz crystal microbalance [22] studies, and threshold electrolyte solution concentrations were identified as $c_s = 0.03$ mol L^{-1} and $c_s = 0.3$ mol L^{-1}, respectively. Below the threshold solution concentrations, measured ΣK values increased with decreasing c_s.

The dependence of ΣK on c_s is illustrated in Figure 8, which compares ΣK values for polyamide films thicker than 5.4 nm as a function of NaCl solution concentration c_s. ΣK is proportional to the quantity $(R_{mem}c_s)^{-1}$ according to Eq. 6, and ΣK values were calculated from Eq. 6 using measured $(R_{mem}c_s)^{-1}$ values for each polyamide film thickness, assuming $D_s = 0.8 \times 10^{-14}$ m^2 s^{-1}, which is the low end of the range of reported NaCl diffusion coefficients in polyamide [19]. Eq. 9 was then fit to the calculated ΣK values from Eq. 6. In fitting Eq. 9, K_s was estimated as the best fit to calculated ΣK values for measurements made in 100 mmol L^{-1} NaCl solution, where membrane fixed charges and associated Donnan partitioning effects are assumed to be screened ($X_{mem} = 0$). The resulting K_s value of 0.016 was fixed in Eq. 9 for all subsequent fits to calculated ΣK values. The membrane fixed charge concentration X_{mem} was iteratively adjusted for individual polyamide film samples to achieve the best fit between Eq. 9 and ΣK values calculated from Eq. 6 for each film across all measured NaCl solution concentrations.
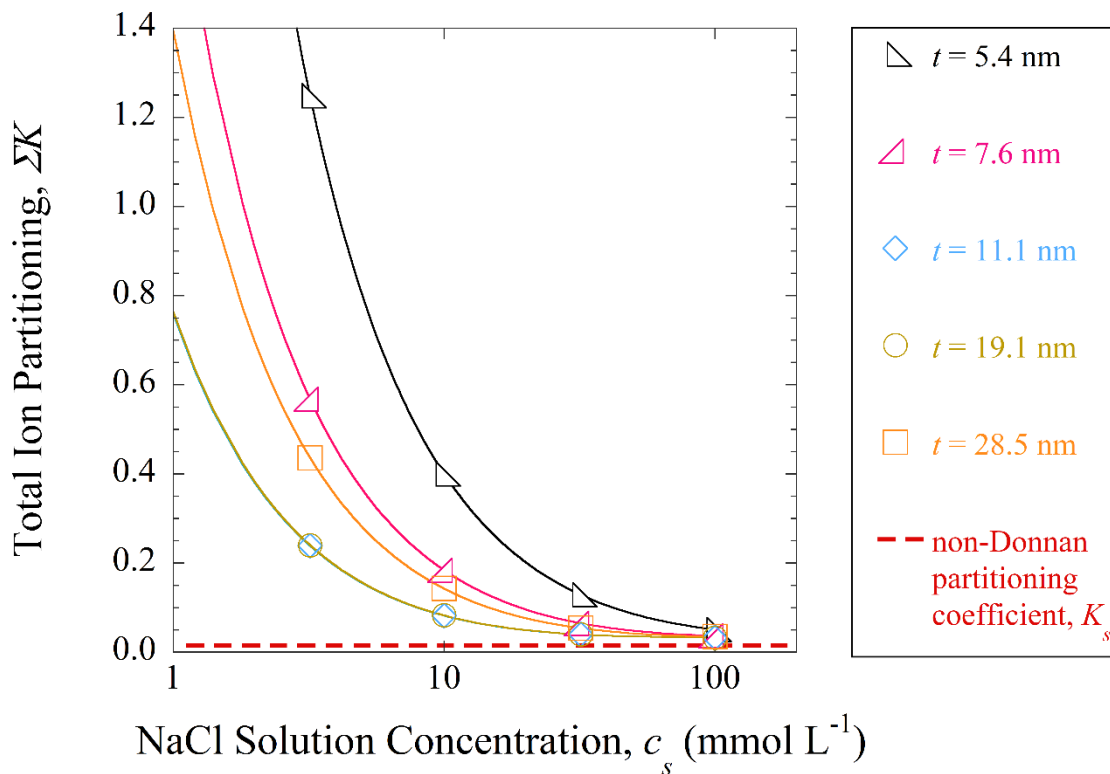
Figure 8 – Total ion partitioning values, ΣK, for polyamide films with different dry thicknesses, t, as a function of NaCl solution concentration, c_s (symbols). The estimated non-Donnan partitioning coefficient, K_s, a component of ΣK, is indicated by the dashed line.

In Figure 8, calculated total ion partitioning ΣK values for polyamide films thicker than 5.4 nm decrease with increasing solution concentration and converge to the range $\Sigma K = 0.033$ to 0.035 at 100 mmol L^{-1} NaCl solution concentration. The fixed membrane charge concentrations X_{mem} for the polyamide films resulting from fitting Eq. 9 to the measured $(R_{mem}c_s)^{-1}$ values range from 0.8 mmol L^{-1} to 4.0 mmol L^{-1}, which is an order of magnitude greater than the concentration on the order of X_{mem} ~0.01 mmol L^{-1} to 0.1 mmol L^{-1} estimated by Freger et al. [23] using a similar analysis for EIS results. An identical fitting procedure was performed for Eq. 9 assuming the high end of the range of reported NaCl diffusion coefficients in polyamide ($D_s = 1.5 \times 10^{-14}$ m^2 s^{-1}) [19], with a resulting salt partition coefficient $K_s = 0.008$.

4.8   Characterizing salt permeability from membrane resistance

Salt permeabilities, P_s, of the polyamide films are calculated from Eq. 10, using the total ion partitioning ΣK values defined in Eq. 6. The calculated salt permeabilities are shown in Figure 9.

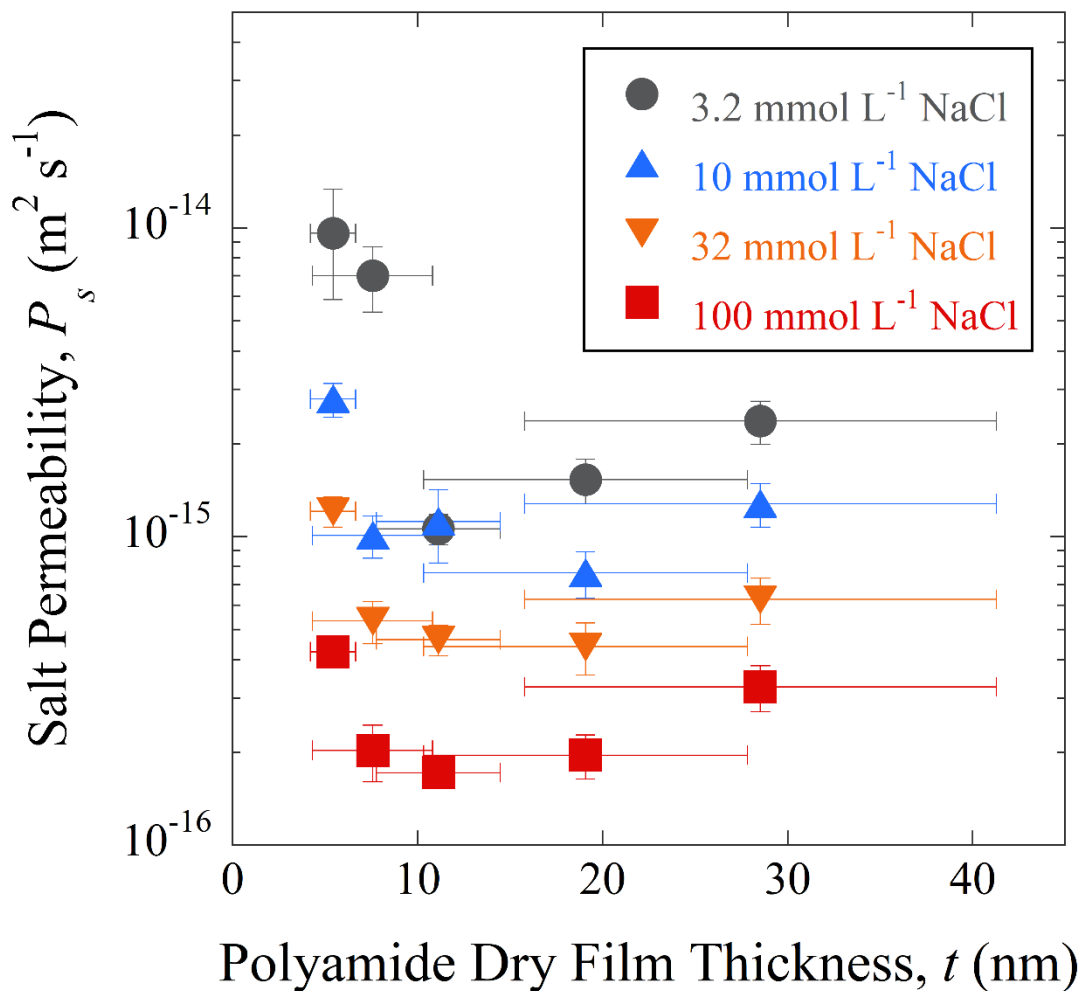$$P_s = D_s \sum K = \frac{t}{c_s R_{mem}} \frac{RT}{F^2} \qquad\qquad \text{(Eq. 10)}$$

Figure 9 – Calculated NaCl salt permeabilities, P_s, as a function of polyamide film thickness, t, for different NaCl solution concentrations.

The calculated salt permeabilities under all conditions are in the range $P_s = 10^{-16}$ m^2 s^{-1} to 10^{-14} m^2 s^{-1}. For each NaCl solution concentration, P_s decreases with increasing polyamide film thickness to $t = 11.1$ nm, and subsequently increases with increasing film thickness to $t = 28.5$ nm. This behavior reflects the trend of non-linear increases in R_{mem} with increasing film thickness and the observed plateau in R_{mem} for films thicker than approximately 19 nm. For each polyamide film thickness, P_s is inversely proportional to NaCl solution concentration c_s and R_{mem} according to Eq. 10. Membrane resistance also has an inverse relationship to solution

concentration, and R_{mem} for thicker films ($t > 10$ nm) is more concentration-dependent than for thinner films ($t < 10$ nm). Thus, the decreasing trend of P_s with increasing solution concentration indicates that for these polyamide films, the increase in c_s has a greater impact on calculated salt permeabilities than corresponding decreases in R_{mem} with increasing c_s. Calculated salt permeabilities at the highest NaCl solution concentration (100 mmol L^{-1}) are in the range $P_s = 1.3 \times 10^{-16}$ m^2 s^{-1} to 3.9×10^{-16} m^2 s^{-1}, which is an order of magnitude less than the salt permeabilities of $P_s = 1.9 \times 10^{-15}$ m^2 s^{-1} to 3.5×10^{-15} m^2 s^{-1} that were measured for polyamide films (MPD and isophthaloyl chloride, IPC) in 1% to 10% by mass NaCl solutions using a pulsed nuclear magnetic resonance technique [19].

Polyamide salt permeabilities may also be compared in the context of the thermodynamic (partition coefficient, K_s) and kinetic (diffusion coefficient, D_s) components of permeability, P_s. Using non-Donnan salt partition coefficients, K_s, estimated for the polyamide films and using the reported range of NaCl diffusion coefficients in polyamide, $D_s = 0.8 \times 10^{-14}$ m^2 s^{-1} to 1.5×10^{-14} m^2 s^{-1} [19], the salt permeability can be calculated as $P_s = D_s K_s$. This non-Donnan salt permeability is descriptive of co-ion permeability in the polyamide film, which is expected to govern salt permeability under high-salinity desalination conditions that are modeled with solution-diffusion theory [36].

The non-Donnan salt partition coefficient K_s determined from EIS measurements for mLbL polyamide films in this work is compared to other experimental measurements of polyamide salt partition coefficients in Table 1. The salt solution concentrations used during measurement of the K_s values in Table 1 are equal to or greater than the 100 mmol L^{-1} NaCl solution concentration used to estimate K_s in this study. Consequently, reported salt partition coefficients are assumed to reflect non-Donnan partitioning. For the previous quartz crystal microbalance [22] and EIS [23] studies, an analysis of Donnan and non-Donnan partitioning was explicitly performed. Recent molecular dynamics simulations of salt rejection by polyamide membranes observed almost no salt partitioning during the timescales and conditions of the simulations [17,37]. However, a relatively larger area membrane simulation was able to characterize a NaCl partition coefficient [42], which is also included in Table 1. A salt partition coefficient less than one is expected for highly rejecting polyamide films [23], and a variety of characterization techniques identified in Table 1 have determined K_s values less than one. The range $K_s = 0.008$ to 0.016 estimated from these EIS measurements is one of the lowest reported values and is consistent with previous EIS [23] and atomic absorption spectroscopy [20] measurements that determined $K_s \approx 0.001$ and $K_s = 0.018$, respectively.

Table 1 – Comparison of salt partition coefficients K_s in polyamide films determined using different characterization methods

Characterization Method	Polyamide Sample	Salt Solution	Salt Partition Coefficient, K_s
Pulsed nuclear magnetic resonance [19]	polyamide film (IPC/MPD)	1% to 10% by mass NaCl	$K_s = 0.2$
Atomic absorption spectroscopy [20]	polyamide film (IPC/MPD)	1% by mass NaCl	$K_s = 0.018$
Rutherford backscattering spectroscopy [21]	commercial polyamide membrane	200 mmol L^{-1} to 500 mmol L^{-1} NaCl	$K_s = 6 \pm 2$
Quartz crystal microbalance [22]	commercial polyamide membrane	300 mmol L^{-1} to 1,000 mmol L^{-1} NaCl	$K_s = 0.12$ to 0.56
Electrochemical impedance spectroscopy [23]	commercial polyamide membrane	500 mmol L^{-1} and 1,000 mmol L^{-1} KCl	$K_s \approx 0.001$
Molecular dynamics simulation [42]	polyamide film (TMC/MPD)	500 mmol L^{-1} NaCl	$K_s = 0.17$ to 0.26
Electrochemical impedance spectroscopy (this work)	polyamide film (TMC/MPD)	100 mmol L^{-1} NaCl	$K_s = 0.008$ to 0.016

To compare salt permeabilities determined from EIS characterization to the salt rejection performance of thin-film composite desalination membranes, a salt permeability coefficient, B (L m^{-2} h^{-1}), is calculated from the measured salt permeability according to Eq. 11.

$$B = \frac{P_s}{t} \qquad\qquad (Eq.\ 11)$$

Manufacturer-provided specifications for commercial, polyamide, thin-film composite, reverse osmosis membranes typically do not identify a salt permeability, P_s, or permeability coefficient, B. Instead, membrane performance is described in terms of salt rejection, which is dependent on experimental conditions. Salt permeability coefficients have been reported in the literature for commercial reverse osmosis membranes [43–46] and for hand-cast, polyamide (TMC/MPD), thin-film composite membranes designed for reverse osmosis desalination [47,7,48]. The salt permeability coefficients for these membranes are in the range 0.1 L m^{-2} h^{-1} to 2.3 L m^{-2} h^{-1}. The individual reported B values and the conditions under which they were measured are summarized in Table S2 of the Supporting information. Figure 10 compares the calculated salt permeability coefficients for polyamide films from this EIS study to the reported values for polyamide thin-film composite membranes. The concentration dependence of salt permeability, P_s, is also reflected in the salt permeability coefficient, B.
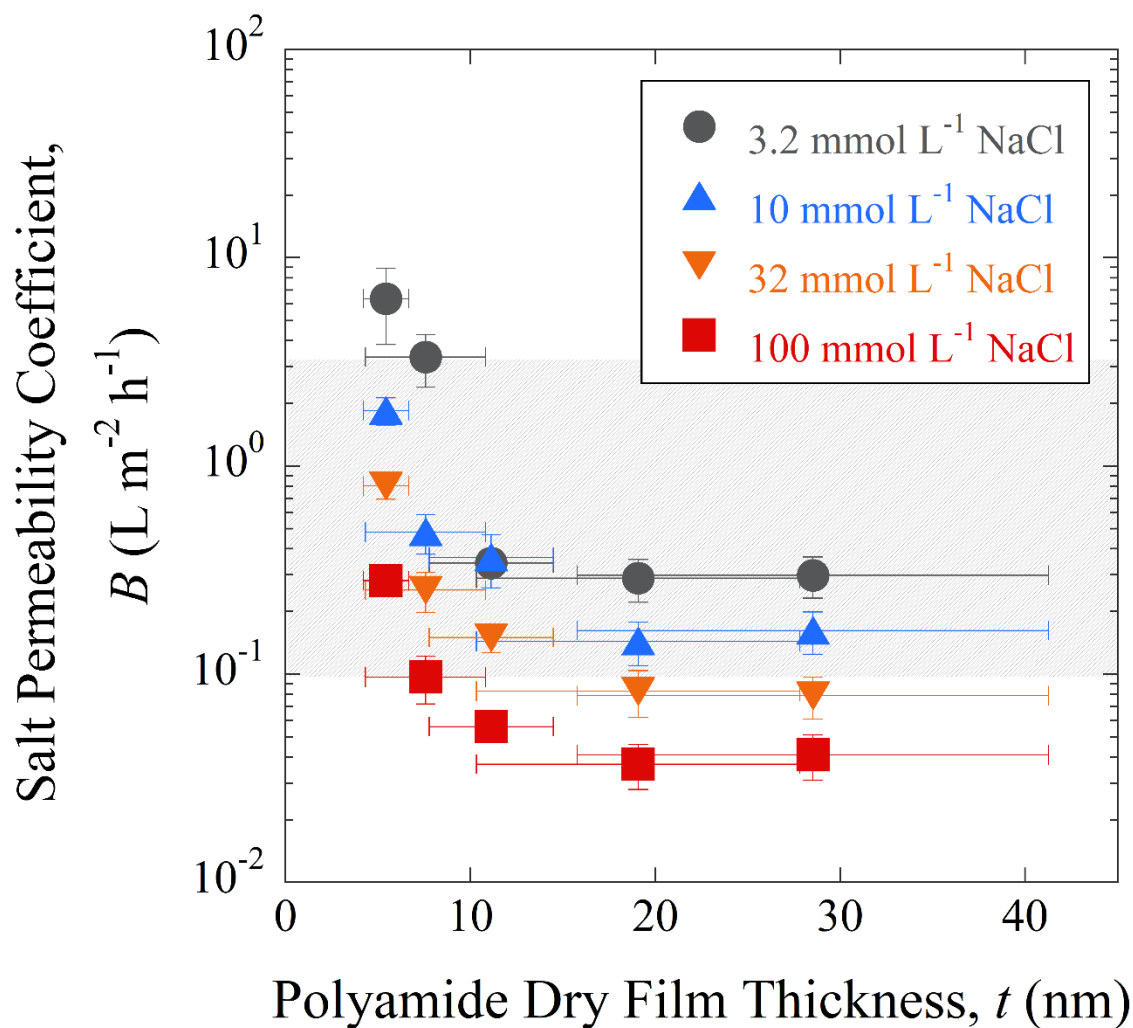
Figure 10 – Salt permeability coefficients, *B,* calculated from EIS characterization as a function of polyamide film thickness, *t* (symbols) compared to reported salt permeability coefficients for polyamide thin-film composite membranes (shaded area).

5   Conclusions

This study demonstrates that EIS enables the measurement of salt permeability in controlled polyamide thin films at solution-diffusion timescales through the measurement of film resistance. The impedance spectra for supported thin polyamide films measured in NaCl solutions are modeled with equivalent circuits that characterize electrode double layer capacitance, solution resistance, and the resistance, R_{mem}, and capacitance, C_{mem}, of the polyamide film, which are

associated with a characteristic low-frequency (RC) response. Membrane capacitance does not demonstrate clear trends with polyamide film thickness or electrolyte solution properties. However, membrane resistance exhibits expected behavior with respect to polyamide film thickness, solution concentration, and solute charge. Thus, R_{mem} is used to characterize total ion partitioning ΣK and the non-Donnan salt partition coefficient K_s for the polyamide films.

Salt permeabilities determined from membrane resistance are in the range $P_s = 1.3 \times 10^{-16}$ m^2 s^{-1} to 3.9×10^{-16} m^2 s^{-1} for the highest NaCl solution concentration studied (100 mmol L^{-1}), which is an order of magnitude less than a reported salt permeability measured using pulsed nuclear magnetic resonance. Salt partition coefficients, K_s, estimated from total ion partitioning ΣK at high solution concentration, are generally lower than previously reported values and are consistent with measurements from atomic absorption spectroscopy and a previous EIS study. Calculated salt permeability coefficients, B, that incorporate polyamide thickness are within the range of reported values for polyamide, thin-film composite, reverse osmosis membranes.

Electrochemical impedance spectroscopy is shown to be a valuable tool for studying salt permeability with the goal of improving membrane permselectivity. Applying EIS to controlled polyamide films fabricated through mLbL deposition overcomes previously reported challenges with EIS characterization of rough, heterogeneous, commercial polyamide membranes. Future work will examine the influence of cation and anion charge on salt permeability and may expand EIS characterization to unsupported polyamide films. Electrochemically active ions may also be introduced to study the diffusion component of salt permeability in these films.

Acknowledgements

References

[1]   H.B. Park, J. Kamcev, L.M. Robeson, M. Elimelech, B.D. Freeman, Maximizing the right stuff: The trade-off between membrane permeability and selectivity, Science. 356 (2017). doi:10.1126/science.aab0530.

[2]   J.R. Werber, C.O. Osuji, M. Elimelech, Materials for next-generation desalination and water purification membranes, Nat. Rev. Mater. 1 (2016) 16018.

[3]   K.P. Lee, T.C. Arnot, D. Mattia, A review of reverse osmosis membrane materials for desalination—Development to date and future potential, J. Membr. Sci. 370 (2011) 1–22. doi:10.1016/j.memsci.2010.12.036.

[4]   J.G. Wijmans, R.W. Baker, The solution-diffusion model: a review, J. Membr. Sci. 107 (1995) 1–21. doi:10.1016/0376-7388(95)00102-I.

[5]   G.M. Geise, H.B. Park, A.C. Sagle, B.D. Freeman, J.E. McGrath, Water permeability and water/salt selectivity tradeoff in polymers for desalination, J. Membr. Sci. 369 (2011) 130–138. doi:10.1016/j.memsci.2010.11.054.

[6]   V. Freger, Nanoscale Heterogeneity of Polyamide Membranes Formed by Interfacial Polymerization, Langmuir. 19 (2003) 4791–4797. doi:10.1021/la020920q.

[7]   A.K. Ghosh, E.M.V. Hoek, Impacts of support membrane structure and chemistry on polyamide–polysulfone interfacial composite membranes, J. Membr. Sci. 336 (2009) 140–148. doi:10.1016/j.memsci.2009.03.024.

[8]   E. Dražević, K. Košutić, V. Freger, Permeability and selectivity of reverse osmosis membranes: Correlation to swelling revisited, Water Res. 49 (2014) 444–452. doi:10.1016/j.watres.2013.10.029.

[9]   F.A. Pacheco, I. Pinnau, M. Reinhard, J.O. Leckie, Characterization of isolated polyamide thin films of RO and NF membranes using novel TEM techniques, J. Membr. Sci. 358 (2010) 51–59. doi:10.1016/j.memsci.2010.04.032.

[10] V. Freger, Swelling and Morphology of the Skin Layer of Polyamide Composite Membranes: An Atomic Force Microscopy Study, Environ. Sci. Technol. 38 (2004) 3168–3175. doi:10.1021/es034815u.

[11] Chan Edwin P., Lee Stephen C., Thickness-dependent swelling of molecular layer-by-layer polyamide nanomembranes, J. Polym. Sci. Part B Polym. Phys. 55 (2017) 412–417. doi:10.1002/polb.24285.

[12] Chan Edwin P., Young Allison P., Lee Jung-Hyun, Chung Jun Young, Stafford Christopher M., Swelling of ultrathin crosslinked polyamide water desalination membranes, J. Polym. Sci. Part B Polym. Phys. 51 (2012) 385–391. doi:10.1002/polb.23235.

[13] N.K. Nadermann, E.P. Chan, C.M. Stafford, Bilayer Mass Transport Model for Determining Swelling and Diffusion in Coated, Ultrathin Membranes, ACS Appl. Mater. Interfaces. 7 (2015) 3492–3502. doi:10.1021/am507091s.

[14] E.P. Chan, Deswelling of ultrathin molecular layer-by-layer polyamide water desalination membranes, Soft Matter. 10 (2014) 2949–2954. doi:10.1039/C4SM00088A.

[15] Y. Jin, W. Wang, Z. Su, Spectroscopic study on water diffusion in aromatic polyamide thin film, J. Membr. Sci. 379 (2011) 121–130. doi:10.1016/j.memsci.2011.05.055.

[16]   Johnson Peter M., Yoon Joonsung, Kelly Jennifer Y., Howarter John A., Stafford Christopher M., Molecular layer-by-layer deposition of highly crosslinked polyamide films, J. Polym. Sci. Part B Polym. Phys. 50 (2011) 168–173. doi:10.1002/polb.23002.

[17]   W. Gao, F. She, J. Zhang, L.F. Dumée, L. He, P.D. Hodgson, L. Kong, Understanding water and ion transport behaviour and permeability through poly(amide) thin film composite membrane, J. Membr. Sci. 487 (2015) 32–39. doi:10.1016/j.memsci.2015.03.052.

[18]   M. Shen, S. Keten, R.M. Lueptow, Dynamics of water and solute transport in polymeric reverse osmosis membranes via molecular dynamics simulations, J. Membr. Sci. 506 (2016) 95–108. doi:10.1016/j.memsci.2016.01.051.

[19]   M.A. Frommer, J.S. Murday, R.M. Messalem, Solubility and diffusivity of water and of salts in an aromatic polyamide film, Eur. Polym. J. 9 (1973) 367–373. doi:10.1016/0014-3057(73)90096-7.

[20]   H. Strathmann, A.S. Michaels, Polymer-water interaction and its relation to reverse osmosis desalination efficiency, Desalination. 21 (1977) 195–202. doi:10.1016/S0011-9164(00)80316-1.

[21]   X. Zhang, D.G. Cahill, O. Coronell, B.J. Mariñas, Partitioning of salt ions in FT30 reverse osmosis membranes, Appl. Phys. Lett. 91 (2007) 181904. doi:10.1063/1.2802562.

[22]   J. Wang, R.S. Kingsbury, L.A. Perry, O. Coronell, Partitioning of Alkali Metal Salts and Boric Acid from Aqueous Phase into the Polyamide Active Layers of Reverse Osmosis Membranes, Environ. Sci. Technol. 51 (2017) 2295–2303. doi:10.1021/acs.est.6b04323.

[23]   S. Bason, Y. Oren, V. Freger, Characterization of ion transport in thin films using electrochemical impedance spectroscopy: II: Examination of the polyamide layer of RO membranes, J. Membr. Sci. 302 (2007) 10–19. doi:10.1016/j.memsci.2007.05.007.

[24]   D.F. Sunday, E.P. Chan, S.V. Orski, R.C. Nieuwendaal, C.M. Stafford, Functional group quantification of polymer nanomembranes with soft x-rays, Phys. Rev. Mater. 2 (2018) 032601. doi:10.1103/PhysRevMaterials.2.032601.

[25]   M.E. Tousley, D.L. Shaffer, J.-H. Lee, C.O. Osuji, M. Elimelech, Effect of Final Monomer Deposition Steps on Molecular Layer-by-Layer Polyamide Surface Properties, Langmuir. 32 (2016) 10815–10823. doi:10.1021/acs.langmuir.6b02746.

[26]   D.L. Shaffer, M.E. Tousley, M. Elimelech, Influence of polyamide membrane surface chemistry on gypsum scaling behavior, J. Membr. Sci. 525 (2017) 249–256. doi:10.1016/j.memsci.2016.11.003.

[27]   T.J. Zimudzi, K.E. Feldman, J.F. Sturnfield, A. Roy, M.A. Hickner, C.M. Stafford, Quantifying Carboxylic Acid Concentration in Model Polyamide Desalination Membranes via Fourier Transform Infrared Spectroscopy, Macromolecules. 51 (2018) 6623–6629. doi:10.1021/acs.macromol.8b01194.

[28]   Equipment and instruments or materials are identified herein to adequately specify the experimental details. Such identification does not imply recommendation by the National Institute of Standards and Technology, nor does it imply the materials are necessarily the best available for the purpose., (n.d.).

[29]   E.P. Chan, J.-H. Lee, J.Y. Chung, C.M. Stafford, An automated spin-assisted approach for molecular layer-by-layer assembly of crosslinked polymer thin films, Rev. Sci. Instrum. 83 (2012) 114102. doi:10.1063/1.4767289.

[30]   Z. Shi, J. Lipkowski, Chloride adsorption at the Au(111) electrode surface, J. Electroanal. Chem. 403 (1996) 225–239. doi:10.1016/0022-0728(95)04313-6.

[31] G. Gotti, D. Evrard, K. Fajerwerg, P. Gros, Oxygen reduction reaction features in neutral media on glassy carbon electrode functionalized by chemically prepared gold nanoparticles, J. Solid State Electrochem. 20 (2016) 1539–1550. doi:10.1007/s10008-016-3159-x.

[32] J.-B. Jorcin, M.E. Orazem, N. Pébère, B. Tribollet, CPE analysis by local electrochemical impedance spectroscopy, Electrochem. Impedance Spectrosc. 51 (2006) 1473–1479. doi:10.1016/j.electacta.2005.02.128.

[33] M. Natrella, NIST/SEMATECH e-Handbook of Statistical Methods, NIST/SEMATECH, 2010. http://www.itl.nist.gov/div898/handbook/.

[34] C.H. Hsu, F. Mansfeld, Technical Note: Concerning the Conversion of the Constant Phase Element Parameter Y0 into a Capacitance, CORROSION. 57 (2001) 747–748. doi:10.5006/1.3280607.

[35] W.M. Haynes, CRC handbook of chemistry and physics, CRC press, 2014.

[36] V. Freger, S. Bason, Characterization of ion transport in thin films using electrochemical impedance spectroscopy: I. Principles and theory, J. Membr. Sci. 302 (2007) 1–9. doi:10.1016/j.memsci.2007.06.046.

[37] M. Shen, S. Keten, R.M. Lueptow, Rejection mechanisms for contaminants in polyamide reverse osmosis membranes, J. Membr. Sci. 509 (2016) 36–47. doi:10.1016/j.memsci.2016.02.043.

[38] B. Tansel, Significance of thermodynamic and physical characteristics on permeation of ions during membrane separation: Hydrated radius, hydration free energy and viscous effects, Sep. Purif. Technol. 86 (2012) 119–126. doi:10.1016/j.seppur.2011.10.033.

[39] G.M. Geise, D.R. Paul, B.D. Freeman, Fundamental water and salt transport properties of polymeric materials, Prog. Polym. Sci. 39 (2014) 1–42. doi:10.1016/j.progpolymsci.2013.07.001.

[40] A.E. Yaroshchuk, V. Ribitsch, The use of trace ions for advanced characterisation of transport properties of NF membranes in electrolyte solutions: theoretical analysis, J. Membr. Sci. 201 (2002) 85–94. doi:10.1016/S0376-7388(01)00706-2.

[41] A. Szymczyk, P. Fievet, Investigating transport properties of nanofiltration membranes by means of a steric, electric and dielectric exclusion model, J. Membr. Sci. 252 (2005) 77–88. doi:10.1016/j.memsci.2004.12.002.

[42] V. Kolev, V. Freger, Molecular Dynamics Investigation of Ion Sorption and Permeation in Desalination Membranes, J. Phys. Chem. B. 119 (2015) 14168–14179. doi:10.1021/acs.jpcb.5b06566.

[43] P. Eriksson, Water and salt transport through two types of polyamide composite membranes, J. Membr. Sci. 36 (1988) 297–313. doi:10.1016/0376-7388(88)80024-3.

[44] E.M. Van Wagner, A.C. Sagle, M.M. Sharma, B.D. Freeman, Effect of crossflow testing conditions, including feed pH and continuous feed filtration, on commercial reverse osmosis membrane performance, J. Membr. Sci. 345 (2009) 97–109. doi:10.1016/j.memsci.2009.08.033.

[45] A.C. Sagle, E.M. Van Wagner, H. Ju, B.D. McCloskey, B.D. Freeman, M.M. Sharma, PEG-coated reverse osmosis membranes: Desalination properties and fouling resistance, J. Membr. Sci. 340 (2009) 92–108. doi:10.1016/j.memsci.2009.05.013.

[46] E.M. Van Wagner, A.C. Sagle, M.M. Sharma, Y.-H. La, B.D. Freeman, Surface modification of commercial polyamide desalination membranes using poly(ethylene glycol) diglycidyl ether to enhance membrane fouling resistance, J. Membr. Sci. 367 (2011) 273–287. doi:10.1016/j.memsci.2010.11.001.

[47] A.K. Ghosh, B.-H. Jeong, X. Huang, E.M.V. Hoek, Impacts of reaction and curing conditions on polyamide composite reverse osmosis membrane properties, J. Membr. Sci. 311 (2008) 34–45. doi:10.1016/j.memsci.2007.11.038.

[48] A. Tiraferri, N.Y. Yip, A.P. Straub, S. Romero-Vargas Castrillon, M. Elimelech, A method for the simultaneous determination of transport and structural parameters of forward osmosis membranes, J. Membr. Sci. 444 (2013) 523–538. doi:10.1016/j.memsci.2013.05.023.

Characterizing salt permeability in polyamide desalination membranes using electrochemical impedance spectroscopy

Supporting Information

Devin L. Shaffer [a], Kathleen E. Feldman [b], Edwin P. Chan [b], Gery R. Stafford [b], Christopher M. Stafford [b]

[a] Civil and Environmental Engineering Department, University of Houston, 4726 Calhoun Road, Houston, TX 77204, USA

[b] Materials Science and Engineering Division, Material Measurement Laboratory, National Institute of Standards and Technology (NIST), 100 Bureau Drive, Gaithersburg, MD 20899, USA

[*] Corresponding author: C.M. Stafford, tel.: 301-975-4368; email: chris.stafford@nist.gov

Supporting Information Contents

Number of pages:	11
Number of figures:	5
Number of tables:	3

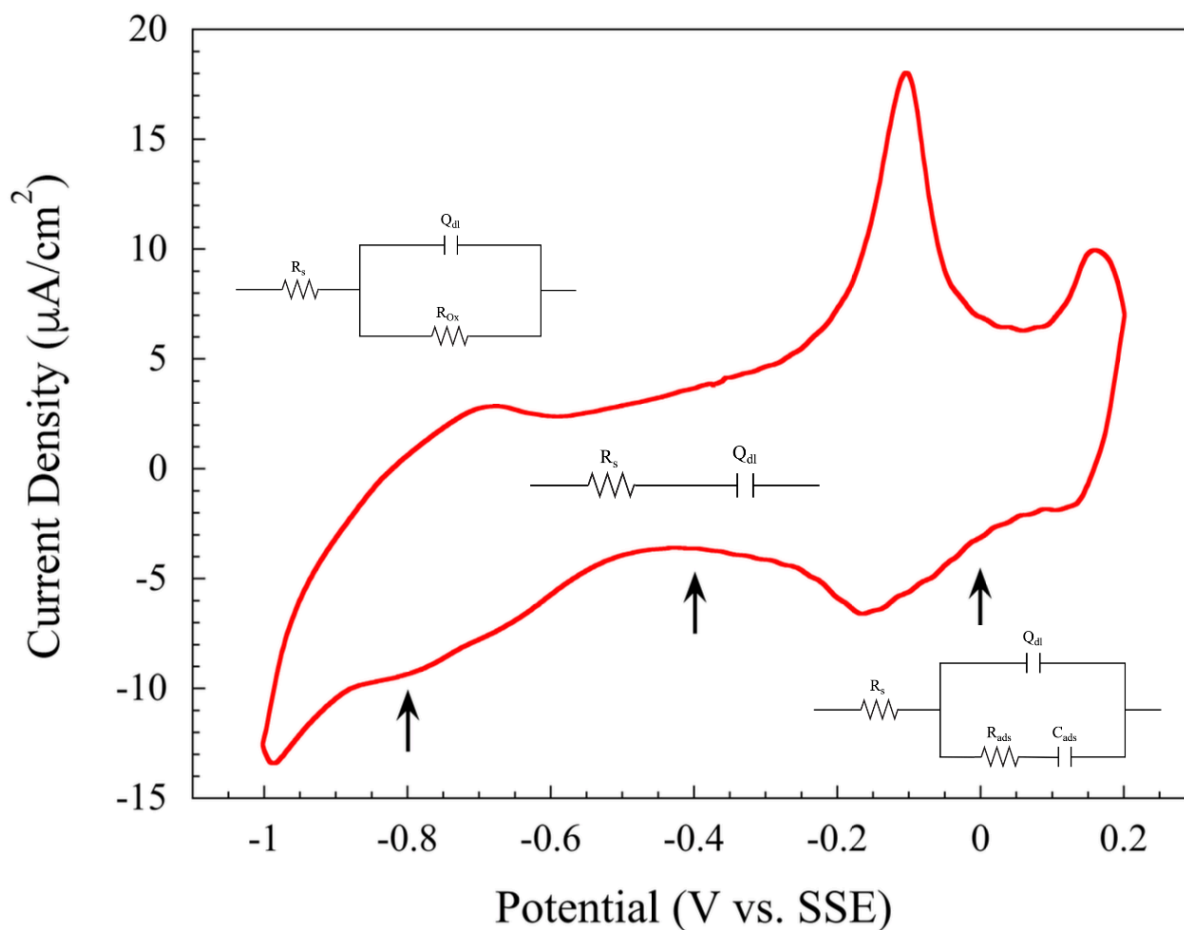## 6 Determination of System Measurement Potential and Associated Equivalent Circuit Model

Figure S1 – Linear sweep voltammogram of a bare gold-coated silicon working electrode in 100 mmol L^{-1} NaCl solution. The reference electrode was a saturated mercury/mercurous sulfate electrode (SSE), and the sweep rate was 100 mV s^{-1}. The arrows depict the potentials at which the electrochemical impedance was measured. The impedance data at each potential were fit to the corresponding equivalent circuit.

Figure S1 shows a voltammetric sweep of a gold-coated silicon electrode using the same three-probe electrochemical cell used for the impedance measurements. The double layer region is observed at a potential of about -0.4 V. The only electrochemical process occurring in this potential region is charging and discharging the gold surface in response to changes in potential.

As the potential is moved in the anodic (positive) direction, a peak in the current is apparent at a potential of -0.1 V SSE. This has been attributed to the specific adsorption of chloride onto the gold surface [1]. The chloride is desorbed when the potential is swept in the negative direction. Gold oxidation occurs at potentials positive of chloride adsorption/desorption. As the potential is moved in the negative direction from the double layer region, oxygen reduction is apparent at potentials ranging from approximately -0.6 V SSE to -1.0 V SSE [2]. The magnitude of this current can be reduced by vigorously sparging the electrolyte solution with argon to remove dissolved oxygen. H_2O reduction to H_2 occurs at more negative potentials.

The electrochemical impedance associated with the double layer region (-0.4 V SSE) is represented by a series $[R_sQ_{dl}]$ circuit where Q_{dl} is a constant phase element depicting the double layer capacitance of the gold electrode, and R_s is the solution resistance between the gold working electrode and the SSE reference electrode. The impedance of the oxygen reduction process that occurs at more negative potentials can be depicted by the same $[R_sQ_{dl}]$ circuit as the double layer region, with an additional resistance (R_{ox}) placed in parallel with Q_{dl} to account for the oxygen reduction reaction. Similarly, the impedance of the chloride adsorption/desorption reaction that occurs at more positive potentials can be depicted by a circuit in which a series $[R_{ads}C_{ads}]$, representing the adsorption process is placed in parallel with Q_{dl}. R_{ads} represents the charge transfer kinetics for chloride adsorption while C_{ads} is required to capture the surface limited nature of the adsorption process. Once a monolayer of chloride is formed on the surface, the adsorption leg effectively becomes an open circuit and the overall impedance is determined by the simple $[R_sQ_{dl}]$ circuit of the double layer.
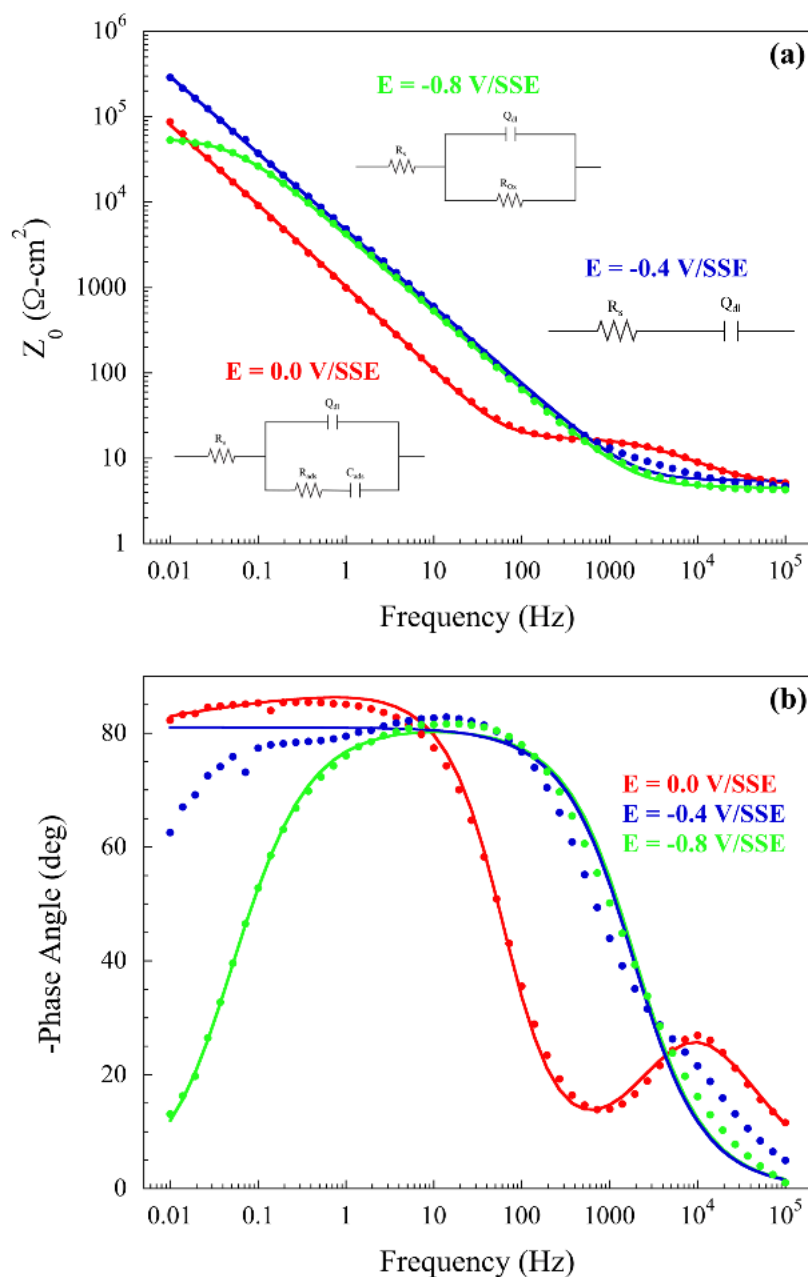
Figure S2 – Bode plots of A) impedance, Z_0, and B) phase angle, ϕ, for the bare gold electrode used in Figure S1 at selected potentials in 100 mmol L^{-1} NaCl solution (symbols) with modeled impedance and phase angle from equivalent circuits identified in the figure (solid lines).

Figure S2 shows the electrochemical impedance for a bare gold electrode in 100 mmol L^{-1} NaCl solution at potentials of 0.0 V SSE, -0.4 V SSE, and -0.8 V SSE. The impedance in the chloride adsorption region at approximately 0.0 V SSE (identified in Figure S1) can be modeled using a $R_s(Q_{dl}[R_{ads}C_{ads}])$ circuit (elements in [brackets] are in series while elements in (parenthesis) are

in parallel). The values of the circuit elements that provide the best fit to the data are listed in Table S1. The R_s values in Table S1 are smaller than those plotted in Fig. 4(A) of the manuscript for the 100 mmol L^{-1} NaCl solution due to different placement of the platinum reference electrode.

Table S1 – Circuit elements obtained from fitting the impedance data in Figure S2.

Potential (V vs SSE)	R_s (Ω-cm^2)	Y_{dl} (μS/cm^2)	n_{dl}	R_{ads} (Ω-cm^2)	C_{ads} (μF/cm^2)	R_{ox} (Ω-cm^2)
0	4.6	33.6	0.76	13.8	136.0	--
-0.4	5.5	40.5	0.90	--	--	--
-0.8	4.5	45.5	0.90	--	--	56,600

The series [$R_{ads}C_{ads}$], placed in parallel with the Q_{dl}, captures the surface limited chloride adsorption reaction. This causes the peak in both Z_0 and ϕ at high frequency. At low frequency, the adsorption leg effectively becomes an open circuit, and the overall impedance is determined by the simple [R_sQ_{dl}] circuit of the double layer. The impedance in the oxygen reduction region at -0.8 V SSE can be modeled using a $R_s(Q_{dl}R_{ox})$ equivalent circuit, where the R_{ox} placed in parallel with Q_{dl} captures the kinetics of the parasitic oxygen reduction reaction. The result is a slight decrease in Z_0 and a significant decrease in ϕ at low frequency (green curves in Figure S2).

In contrast, the double layer region at -0.4 V SSE can be effectively represented by a simple series [R_sQ_{dl}] circuit. At high frequency, Q_{dl} is essentially a short circuit and the impedance is primarily due to R_s. Figure S2(A) clearly shows that Z_0 approaches the value of R_s at high frequency. For this reason, high frequency data is necessary in order to isolate the value of R_s. Although a simple series [R_sQ_{dl}] circuit effectively captures the impedance response in the double layer region (E = -0.4 V SSE), the phase angle deviates from the actual data at low and high frequency. The low frequency deviation is an indication that some parasitic reactions are present, even in the double layer region. However, the reaction rates are extremely slow, otherwise a decrease in Z_0 would be observed, like that seen for the oxygen reduction reaction. The high frequency deviation is likely a high frequency artifact caused by the impedance of the measuring circuit, such as the instrumentation, cables, and leads.

The data shown in Figures S1 and S2 clearly show that minimum electrochemical interference from the gold-coated silicon substrate is obtained at a potential of -0.4 V SSE. For this reason, the impedance of the mLbL polyamide films was measured at a steady-state potential of -0.4 V SSE. At this fixed potential, the gold substrate and the solution between the gold working electrode and the reference electrode are represented with a series [R_sQ_{dl}] circuit.

7   Distinguishing Polyamide Film Response from Bare Gold Electrode Response

With the response of the bare gold electrode modeled as a series [R_sQ_{dl}] circuit, the polyamide film can then be represented by a series of parallel (R_1Q_1) circuits, one for each time constant associated with the membrane, as described in Section 3.2 and Figure 3 of the manuscript. A direct comparison of the impedance response of a bare gold electrode with that of a polyamide-coated gold electrode is shown in Figure S3.

The impedance of the polyamide films (Figure S3(A)) deviates from that of the gold substrate in the frequency range of 1 Hz to 10 kHz. The occurrence of polyamide film impedance at frequencies intermediate to those of double-layer capacitance and solution resistance indicates that the dielectric polarization of the polyamide film happens at a timescale faster than the charging/discharging of the electrode double layer but slower than the transfer of charge by ions in solution that characterizes solution resistance. At low frequency, the impedance is dictated by the double layer capacitance of the gold electrode, Q_{dl}. As shown in Figure S3, the bare gold electrode and the polyamide-covered gold electrode have similar values of Q_{dl}. At high frequency, the impedance should extrapolate to a value equal to R_s. The impedance values for the bare gold and the polyamide-coated gold electrodes are similar (24 Ω-cm^2 and 18 Ω-cm^2, respectively) but they are not identical. Possible reasons for this difference are discussed in Section 4.1 of the manuscript. The occurrence of polyamide film impedance at intermediate frequencies to those of low-frequency double-layer capacitance and high-frequency solution resistance indicates that the dielectric polarization of the polyamide film occurs at a time scale faster than the charging/discharging of the double layer of the gold-coated electrode but slower than the transfer of charge by ions in solution that characterizes solution resistance.

Figure S3(B) is a plot of the phase angle for the bare gold and the polyamide-coated gold electrodes. The bare gold shows the single transition expected for a series [RQ] circuit, from resistance-control ($\phi = 0°$) at high frequency to capacitance-control ($\phi = 90°$) at low frequency. In contrast, the polyamide-coated electrode shows two time constants in the frequency range where the impedance is dominated by the membrane. For this reason, an equivalent electrical circuit with two time constants was used to fit the data. Although the simple series [R_sQ_{dl}] circuit used to model the impedance of the bare gold electrode deviates from the experimental phase angle at high and low frequencies, the phase angle behavior of the polyamide-coated electrode is captured over the entire frequency range using the equivalent circuit with two time constants shown in Figure S3(A). The two time constants for the relatively thick polyamide films are hypothesized to reflect a two-layer polyamide film structure that results from the mLbL growth process, as discussed in Section 4.2.
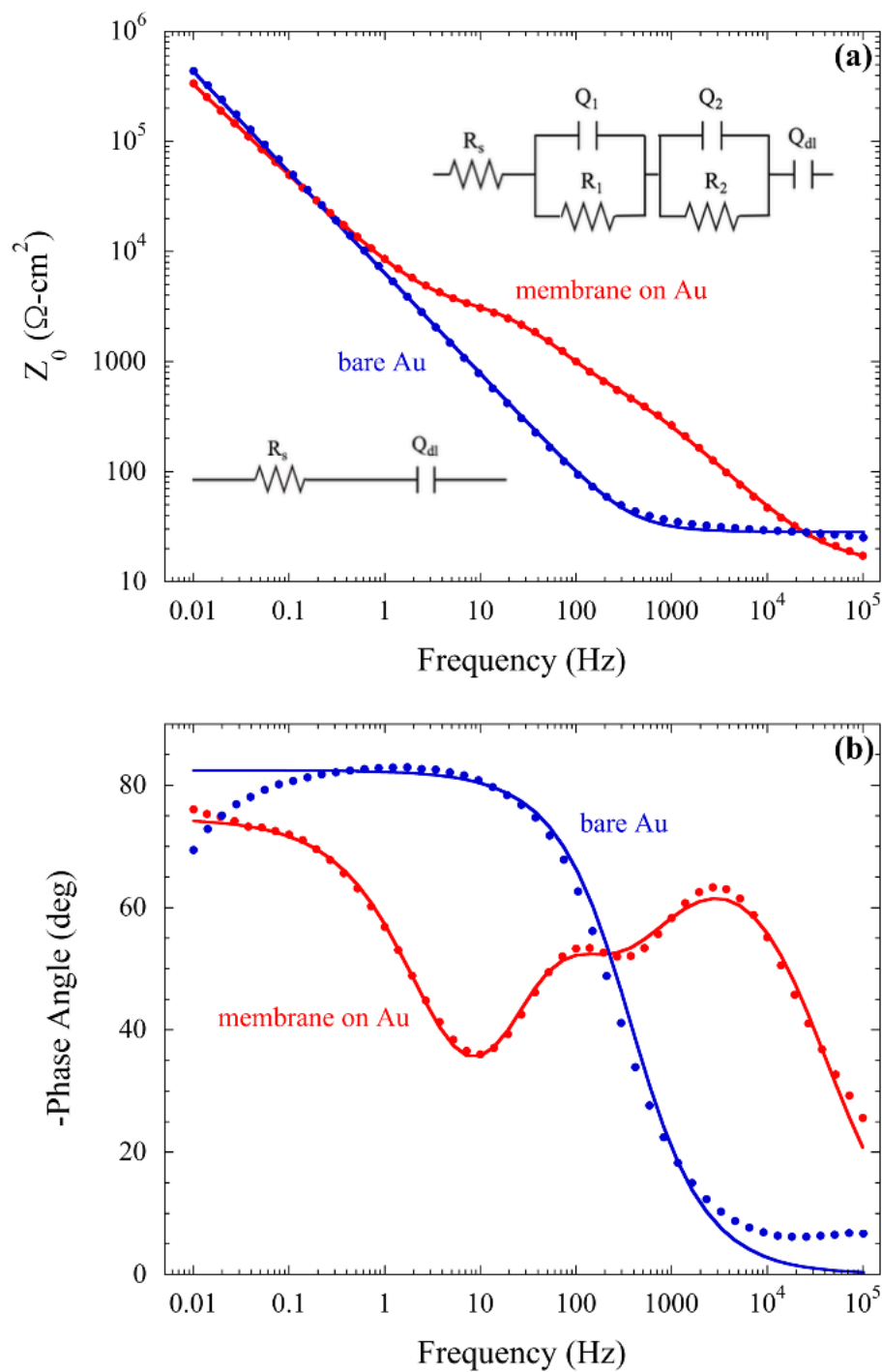
Figure S3 – Bode plots of A) impedance, Z_0, and B) phase angle, ϕ, for the bare gold electrode (blue) and gold electrode coated with a 28.5 nm thick polyamide film (red) in 100 mmol L^{-1} NaCl solution (symbols). Both measurements were made at a steady-state potential of -0.4 V SSE. The solid lines represent the fits to the data using the equivalent circuits identified in the figure.
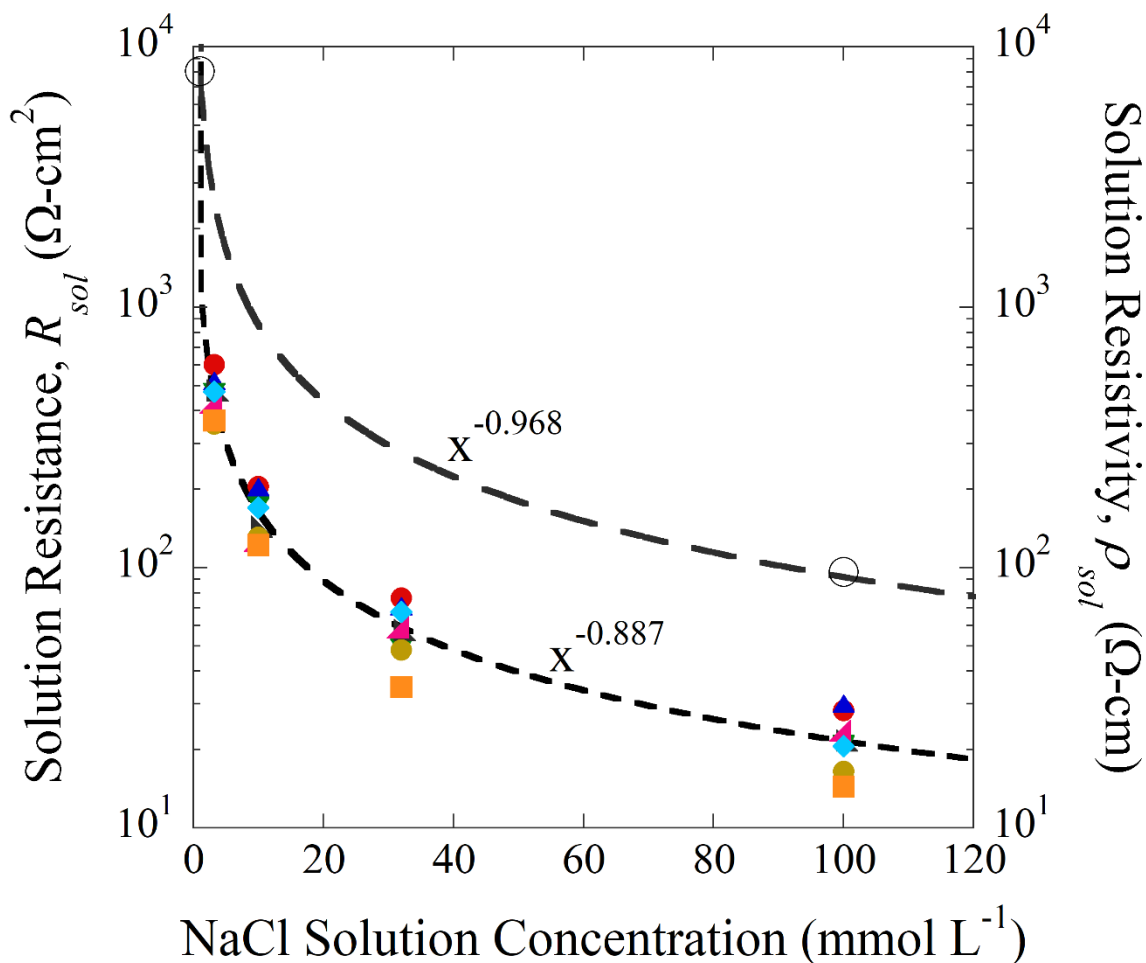
8   Solution Resistance

Figure S4 – NaCl solution resistance from electrochemical impedance spectroscopy measurements, R_{sol} (closed symbols, left vertical axis), and NaCl solution resistivity measurements made using electrochemical impedance spectroscopy and a conductivity cell with a known cell constant, ρ_{sol} (open circles, right vertical axis), as functions of NaCl solution concentration. The short-dash line is a power law fit to R_{sol} data, and the long-dash line is a power-law fit to ρ_{sol} data calculated from equivalent NaCl solution conductivities reported in the literature [3]. Electrochemical impedance spectroscopy measurements of R_{sol} were made with polyamide films deposited on the gold working electrode. Multiple R_{sol} values at a single NaCl solution concentration were determined from equivalent circuit fits to the impedance spectra for impedance measurements made for different polyamide film thicknesses at that NaCl solution concentration.
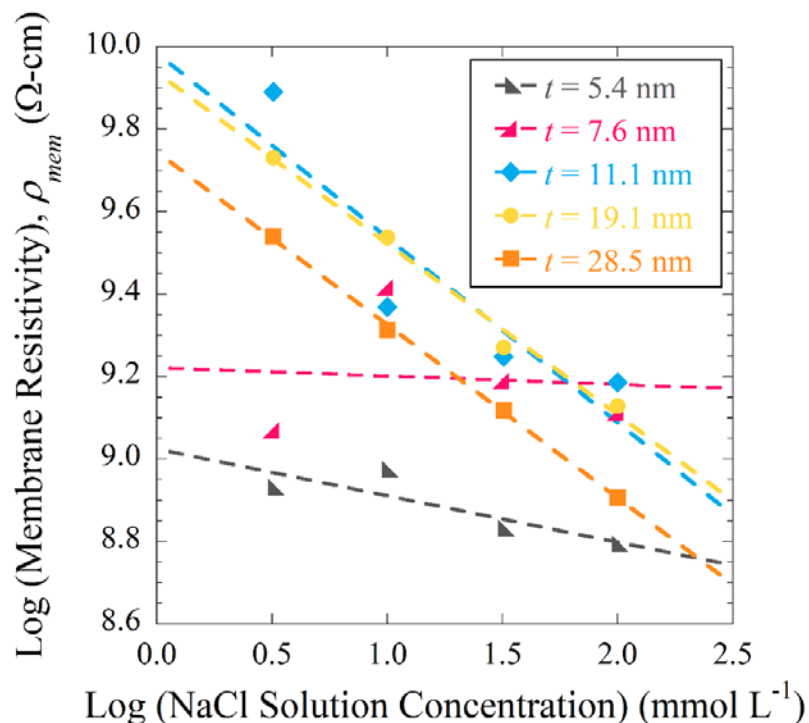
9   Membrane Resistivity

Figure S5 – Logarithm of membrane resistivity, ρ_{mem}, versus logarithm of NaCl solution concentration for polyamide films of different dry thicknesses, t (symbols). Dashed lines are linear fits to ρ_{mem} values for each film thickness.

Table S2 – Extrapolated membrane resistivity, ρ_{mem}, values at 0 mmol L^{-1} NaCl solution concentration for polyamide films of different dry thicknesses, t.

Dry Film Thickness, t (nm)	Log (Membrane Resistivity) at 0 mmol L^{-1} NaCl Solution Concentration, ρ_{mem} (Ω-cm)	R^2 Value for Linear Fit to Log (Membrane Resistivity) versus Log (NaCl Solution Concentration)	Membrane Resistivity at 0 mmol L^{-1} NaCl Solution Concentration, ρ_{mem} (Ω-cm)
5.4	9.02	0.732	1.05×10^9
7.6	9.22	0.928	1.66×10^9
11.1	9.99	0.809	9.77×10^9
19.1	9.94	0.989	8.71×10^9
28.5	9.74	0.999	5.50×10^9

10 Salt Permeability Coefficients

Table S3 – Summary of reported salt permeability coefficients, B, and associated measurement conditions for hand-cast and commercial polyamide thin-film composite membranes for reverse osmosis desalination.

Polyamide Thin-Film Composite Membrane	Salt Permeability Coefficient, B (L m^{-2} h^{-1})	Measurement Conditions	Reference
Hand-cast membrane (isopar organic solvent)	0.50 to 0.78	15.5 bar 2,000 mg L^{-1} NaCl (34 mmol L^{-1} NaCl)	[4]
Hand-cast membrane (pure polysulfone supports)	1.8 and 2.3	15.5 bar 2,000 mg L^{-1} NaCl (34 mmol L^{-1} NaCl)	[5]
Hand-cast polyamide membrane	0.09 to 0.11	27.6 bar 50 mmol L^{-1} NaCl	[6]
Dow LE RO membrane	0.51	10.3 bar 2,000 mg L^{-1} NaCl (34 mmol L^{-1} NaCl)	[7]
Dow XLE RO membrane	1.3	10.3 bar 2,000 mg L^{-1} NaCl (34 mmol L^{-1} NaCl)	[7]
Dow LE RO membrane	1.1	10.3 bar 2,000 mg L^{-1} NaCl (34 mmol L^{-1} NaCl)	[8]
Dow XLE RO membrane	1.7	10.3 bar 2,000 mg L^{-1} NaCl (34 mmol L^{-1} NaCl)	[8]
GE AG RO membrane	0.69	15.5 bar 2,000 mg L^{-1} NaCl (34 mmol L^{-1} NaCl)	[8]
GE AG RO membrane	0.5	15.5 bar 2,000 mg L^{-1} NaCl (34 mmol L^{-1} NaCl)	[9]
FilmTec SW 30 membrane	0.10 to 0.30	10 bar to 70 bar 0.34 g L^{-1} NaCl to 15.9 g L^{-1} NaCl (5.8 mmol L^{-1} NaCl to 270 mmol L^{-1} NaCl)	[10]

References

[1] Z. Shi, J. Lipkowski, Chloride adsorption at the Au(111) electrode surface, Journal of Electroanalytical Chemistry. 403 (1996) 225–239. doi:10.1016/0022-0728(95)04313-6.

[2] G. Gotti, D. Evrard, K. Fajerwerg, P. Gros, Oxygen reduction reaction features in neutral media on glassy carbon electrode functionalized by chemically prepared gold nanoparticles, Journal of Solid State Electrochemistry. 20 (2016) 1539–1550. doi:10.1007/s10008-016-3159-x.

[3] W.M. Haynes, CRC handbook of chemistry and physics, CRC press, 2014.

[4] A.K. Ghosh, B.-H. Jeong, X. Huang, E.M.V. Hoek, Impacts of reaction and curing conditions on polyamide composite reverse osmosis membrane properties, Journal of Membrane Science. 311 (2008) 34–45. doi:10.1016/j.memsci.2007.11.038.

[5] A.K. Ghosh, E.M.V. Hoek, Impacts of support membrane structure and chemistry on polyamide–polysulfone interfacial composite membranes, Journal of Membrane Science. 336 (2009) 140–148. doi:10.1016/j.memsci.2009.03.024.

[6] A. Tiraferri, N.Y. Yip, A.P. Straub, S. Romero-Vargas Castrillon, M. Elimelech, A method for the simultaneous determination of transport and structural parameters of forward osmosis membranes, Journal of Membrane Science. 444 (2013) 523–538. doi:10.1016/j.memsci.2013.05.023.

[7] E.M. Van Wagner, A.C. Sagle, M.M. Sharma, Y.-H. La, B.D. Freeman, Surface modification of commercial polyamide desalination membranes using poly(ethylene glycol) diglycidyl ether to enhance membrane fouling resistance, Journal of Membrane Science. 367 (2011) 273–287. doi:10.1016/j.memsci.2010.11.001.

[8] E.M. Van Wagner, A.C. Sagle, M.M. Sharma, B.D. Freeman, Effect of crossflow testing conditions, including feed pH and continuous feed filtration, on commercial reverse osmosis membrane performance, Journal of Membrane Science. 345 (2009) 97–109. doi:10.1016/j.memsci.2009.08.033.

[9] A.C. Sagle, E.M. Van Wagner, H. Ju, B.D. McCloskey, B.D. Freeman, M.M. Sharma, PEG-coated reverse osmosis membranes: Desalination properties and fouling resistance, Journal of Membrane Science. 340 (2009) 92–108. doi:10.1016/j.memsci.2009.05.013.

[10] P. Eriksson, Water and salt transport through two types of polyamide composite membranes, Journal of Membrane Science. 36 (1988) 297–313. doi:10.1016/0376-7388(88)80024-3.